



A review of the wave gradiometry method for seismic imaging

Chuntao Liang, Feihuang Cao, Zhijin Liu, Yingna Chang

Citation: Liang CT, Cao FH, Liu ZJ, Chang YN (2023). A review of the wave gradiometry method for seismic imaging. *Earthquake Science*, 36(3): 254–281, doi: [10.1016/j.eqs.2023.04.002](https://doi.org/10.1016/j.eqs.2023.04.002)

View online: <http://www.equsci.org.cn/article/doi/10.1016/j.eqs.2023.04.002>

Related articles that may interest you

High-resolution crustal velocity imaging using ambient noise recordings from a high-density seismic array: An example from the Shangrao section of the Xinjiang basin, China

Earthquake Science. 2018, 31(5–6), 242 <https://doi.org/10.29382/eqs-2018-0242-4>

Imaging shallow structure with active-source surface wave signal recorded by distributed acoustic sensing arrays

Earthquake Science. 2018, 31(4), 208 <https://doi.org/10.29382/eqs-2018-0208-4>

Crustal and upper mantle structure beneath Abaga area in Inner Mongolia revealed by Rayleigh-wave phase velocity tomography

Earthquake Science. 2019, 32(5–6), 207 <https://doi.org/10.29382/eqs-2019-0207-03>

Seismic phase picking in China Seismic Array using a deep convolutional neuron network

Earthquake Science. 2020, 33(2), 72 <https://doi.org/10.29382/eqs-2020-0072-03>

Effect of uneven noise source and/or station distribution on estimating the azimuth anisotropy of surface waves

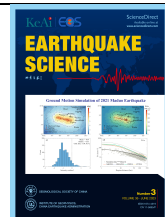
Earthquake Science. 2018, 31(4), 175 <https://doi.org/10.29382/eqs-2018-0175-1>

Bayesian Markov chain Monte Carlo inversion for anisotropy of PP-and PS-wave in weakly anisotropic and heterogeneous media

Earthquake Science. 2017, 30(1), 33 <https://doi.org/10.1007/s11589-017-0173-8>



Follow Earthq Sci WeChat public account for more information



Review

A review of the wave gradiometry method for seismic imaging

Chuntao Liang^{1,2}, Feihuang Cao^{1,✉}, Zhijin Liu¹ and Yingna Chang³¹ Key Laboratory of Earth Exploration and Information Techniques of the China Ministry of Education, Chengdu 610059, China² State Key Laboratory of Oil and Gas Reservoir Geology and Exploration, Chengdu 610059, China³ Exploitation and Development Research Institute, Northwest Oilfield Branch of Sinopec, Urumqi 830000, China**Key points:**

- The technical development of the wave gradiometry method (WGM) is described.
- The theoretical background and major applications of the WGM are discussed.
- Future development of the WGM is summarized.

A B S T R A C T

As dense seismic arrays at different scales are deployed, the techniques to make full use of array data with low computing cost become increasingly needed. The wave gradiometry method (WGM) is a new branch in seismic tomography, which utilizes the spatial gradients of the wavefield to determine the phase velocity, wave propagation direction, geometrical spreading, and radiation pattern. Seismic wave propagation parameters obtained using the WGM can be further applied to invert 3D velocity models, Q values, and anisotropy at lithospheric (crust and/or mantle) and smaller scales (e.g., industrial oilfield or fault zone). Herein, we review the theoretical foundation, technical development, and major applications of the WGM, and compared the WGM with other commonly used major array imaging methods. Future development of the WGM is also discussed.

Keywords: seismic imaging; wave gradiometry method; spatial gradients; phase velocity; anisotropy.**Citation:** Liang CT, Cao FH, Liu ZJ and Chang YN (2023). A review of the wave gradiometry method for seismic imaging. *Earthq Sci* 36(3): 254–281, doi: 10.1016/j.eqs.2023.04.002.

1. Introduction

Seismic arrays at different scales have been deployed worldwide for various purposes. On regional scales, the USArray (Burdick et al., 2008; Krischer et al., 2018;

Bissig et al., 2021), ChinArray (Liu QY et al., 2008, 2014; Zhang L et al., 2020), and AlpArray (Hetényi et al., 2018; Kästle et al., 2022) were deployed to study the deep structures of the continents beneath the United States, China, and Alpine mountains (From Nice in France in the

✉ Corresponding author. Cao FH, email: cfh37@outlook.com

Article history:

Received 22 September 2022

Received in revised form 20 February 2023

Accepted 1 March 2023

Available online 27 March 2023



Production and Hosting by Elsevier on behalf of KeAi

© 2023 The Authors. Publishing services by Elsevier B.V. on behalf of KeAi Communications Co. Ltd. This is an open access article under the CC BY-NC-ND license (<http://creativecommons.org/licenses/by/4.0/>).

<https://doi.org/10.1016/j.eqs.2023.04.002>

west to the Vienna Basin in the east), respectively. Numerous local seismic arrays have also been deployed to address local tectonic problems related to subduction zones, orogenies, and large faults, among others (Lippitsch et al., 2003; Molinari et al., 2016; Chen CX et al., 2017; Porter et al., 2016; Chang YN et al., 2022). Dense seismic arrays at even smaller scales have been deployed for oil, gas, and other mineral resource exploration (Kim et al., 1997; Savazzi and Spagnolin, 2009; De Ridder and Curtis, 2017; Wang Y et al., 2022), hydraulic fracturing monitoring (Keranen et al., 2014; Yang W et al., 2021), and engineering applications (Park et al., 1999; Xia JH et al., 1999).

The increased array density makes it possible to compute spatial gradients of the wavefield more precisely, and thus to use the wave equation directly in imaging subsurface. The wave gradiometry method (WGM) is one of the new techniques to make full use of array data to find phase velocity, azimuth, radiation pattern and geometrical spreading. A variety of methods have been used to process data from seismic arrays. In the oil and gas industry, the arrays are sufficiently dense to use migration techniques to image the subsurface (Kim et al., 1997). However, such methods are not often applicable for global or regional seismology, owing to the uneven distribution of seismic sources and arrays, as well as sparse deep sampling. In these cases, methods such as travel time tomography (Aki and Lee, 1976; Aki et al., 1977), full waveform tomography (Tromp, 2020), surface wave inversion (Xia JH et al., 1999), ambient noise tomography (Shapiro et al., 2005; Bensen et al., 2008), receiver functions (Vinnik, 1977; Langston, 1979; Ammon et al., 1989), shear wave splitting (Gao SS and Liu KH, 2009), and Eikonal tomography (Lin FC et al., 2009) have been applied to study the lithosphere at different scales. For most of these methods (i.e., travel time tomography, waveform tomography, receiver functions, and shear wave splitting), data collected at each station in the array are treated as a point measurement. For some techniques, the wave amplitudes are not used or are treated as secondary information (e.g., in travel time tomography, receiver functions, and shear wave splitting).

Surface waves are frequently used for analysis owing to their high signal-to-noise ratios. For example, surface waves may be inverted to investigate 1D structures along the ray path, and the 1D structures along different paths are then combined to form a 3D model using waveform tomography (Van Der Lee and Nolet, 1997). In addition, group velocity and phase velocity dispersion curves can be measured and inverted to produce a 1D model of a grid, and 1D models for all grids are combined to construct a 3D

model (Knopoff et al., 1966; Barmin et al., 2001; Herrmann and Ammon, 2004; Fischer et al., 2005; Yao HJ et al., 2006; Liang CT and Langston, 2009). In waveform tomography, waveform modeling is often very time-consuming, particularly for high-frequency waves. Dispersion curve-based methods are the most commonly used; however, the methods used to extract dispersion curves vary widely, including the one or two-station methods (Campillo and Paul, 2003; Yang YJ et al., 2007; Fang HJ et al., 2015) and Eikonal and Helmholtz tomographic methods (Lin FC et al., 2009; Lin FC and Ritzwoller, 2011; Qiu HR et al., 2019). The mainstream application of the WGM is also based on dispersion curves (Liang CT and Langston, 2009; Porter et al., 2016).

Eikonal and Helmholtz tomographic methods were developed recently to process array data. These methods obtain the surface wave travel times by tracking the isochronal wavefront and phase velocity dispersion curves are obtained using the Eikonal (Lin FC et al., 2009) and Helmholtz equations (Lin CF and Ritzwoller, 2011), respectively. Both methods are based on the second derivative of the travel time field. Geometrical spreading is considered in Helmholtz tomography, but radiation patterns are not considered in either method.

Langston (2007a, b, c) proposed the WGM to extract the phase velocity, wave directionality, geometrical spreading, and radiation pattern of a wave field. Early publications that applied the WGM ignored the attenuation term in the amplitude variation; thus, the spatial amplitude gradient is collectively called geometrical spreading. The WGM can be applied to the entire wavefield, including body and surface waves. Currently, most applications of the WGM have focused on surface waves, owing to their large amplitudes. Using waveforms from only one earthquake, the WGM can produce local phase velocity maps that cover the entire array. In addition, the amplitude variations estimated by the WGM may be of special use for investigating the attenuation of the structure.

The WGM had been proposed in years and it has been well applied in increasingly more cases. For readers to capture its basic theory and to learn possible applications, here we outline the technical development of the WGM, its theoretical background, and major applications, and compare its usage with those of other techniques. Future development of the WGM is also discussed.

2. WGM technical development history

Since its introduction to seismology by Langston (2007a, b, c), the WGM has undergone a series of

technical developments and has been applied to a wide range of datasets for different purposes. Figure 1 shows the major technical development history of the WGM.

In 2007, Langston published a series of studies that used wavefield spatial gradients to obtain the phase velocity and geometrical spreading for a 1D array (Langston, 2007a), and the wave propagation direction and radiation pattern for a 2D array in the frequency (Langston, 2007b) and time (Langston, 2007c) domains. The WGM is so named because wavefield gradients are the core of the technique. Langston (2007a) showed that if a seismic source is aligned along a linear array, it is possible to compute the spatial gradient (du/dr) of the waveform and further obtain the phase velocity and geometrical spreading. Owing to the absence of information in another dimension, a 1D array cannot constrain the azimuthal propagation properties of seismic waves. Langston (2007b) also derived the formula for using a regular 2D array to compute the 2D spatial gradients ($\partial u/\partial x, \partial u/\partial y$) and to obtain the wave directionality (propagation direction) and radiation pattern in addition to phase velocity and geometrical spreading. However, the finite difference method (Langston, 2007b) is only suitable for regular arrays, and a 2D irregular array may increase the truncation errors of the spatial wavefield gradients.

Langston and Liang CT (2008) used the WGM to compute the rotational component of a wave field. The results indicated that a seismic array with three component instruments can be used as a rotation meter. By rotating the horizontal component waveforms into the radial and transverse directions, which are assumed to be the X and Y directions ($\partial u_x/\partial x, \partial u_y/\partial y$), the four spatial gradients can be used to obtain the second-order strain and rotation tensors as follows:

$$\text{strain} = \begin{pmatrix} \frac{\partial u_x}{\partial x} & \frac{1}{2} \left(\frac{\partial u_x}{\partial y} + \frac{\partial u_y}{\partial x} \right) \\ \frac{1}{2} \left(\frac{\partial u_x}{\partial y} + \frac{\partial u_y}{\partial x} \right) & \frac{\partial u_y}{\partial y} \end{pmatrix}, \quad (2-1)$$

$$\text{rotation} = \begin{pmatrix} 0 & \frac{1}{2} \left(\frac{\partial u_x}{\partial y} - \frac{\partial u_y}{\partial x} \right) \\ \frac{1}{2} \left(\frac{\partial u_y}{\partial x} - \frac{\partial u_x}{\partial y} \right) & 0 \end{pmatrix}. \quad (2-2)$$

Based on USAArray data from the western US, Liang CT and Langston (2009) introduced the weighted inversion method to compute the spatial gradients for an irregular array (described in section 3.2.1). This method makes the WGM applicable to any array with arbitrary geometry and was the first application of the method to a regional array with an average station spacing of 70 km.

Unlike Liang CT and Langston (2009), Poppeliers

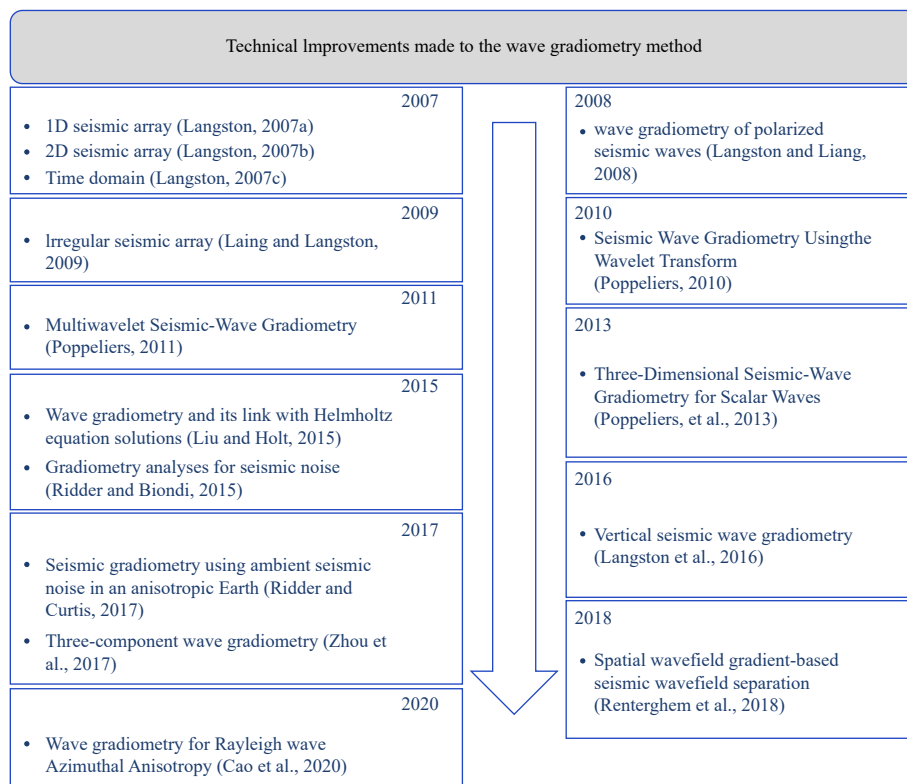


Figure 1. History of the technical development of the wave gradiometry method (WGM).

(2010, 2011) suggested using wavelet and multi-wavelet transforms to process the waveform data before applying the WGM. Poppeliers et al. (2013) then derived a theoretical WGM for a 3D array.

Unlike the time domain WGM based on Hilbert transform (Langston, 2007c), Liu YY and Holt (2015) proposed a linear inversion method to solve the wave gradient coefficients which used for estimating phase velocity. Referencing the Helmholtz tomography, they also introduced an amplitude correction term to the phase velocity (described in sections 3.3.3 and 5.2).

De Ridder and Biondi (2015) proposed using the second spatial derivative of the waveform to directly obtain the phase velocity. In the frequency domain, the wave equation can be written as follows:

$$c^2(\mathbf{r}, \omega) \nabla^2 \widehat{u}(\mathbf{r}, \omega) + \omega^2 \widehat{u}(\mathbf{r}, \omega) = 0, \quad (2-3)$$

where c and ω are the phase velocity and angular frequency, respectively; $\widehat{u}(\mathbf{r}, \omega)$ is the Fourier transformed dual of the waveform (u) at the location \mathbf{r} ; and the Laplacian $\nabla^2 \widehat{u}(\mathbf{r}, \omega)$ is the second spatial derivative of the Fourier transform of the waveform. The second term on the left side of equation (2.3) is the second temporal derivative. Thus, the square of the phase velocity may be obtained by linear regression of the second-order spatial and temporal derivatives. The main challenge in this method is calculating the second order spatial derivative, which may require more stations than the first order spatial derivative.

Langston and Ayele (2016) applied the WGM to a vertical array along the San Andreas Fault Observatory at Depth (SAFOD). The method was shown to be a powerful tool for inverting impedance profiles, and the results were consistent with logging measurements (Langston and Ayele, 2016). This work showed the possibility of applying the WGM to very large volumes of downhole seismic data, particularly for distributed acoustic sensing (DAS) data collected in the oil and gas industry.

Maeda et al. (2016) introduced a wavefield gridding method that can be used to obtain both the waveform and the spatial wavefield gradients at the reference location where a waveform is not recorded (described in section 3.2.2). Porter et al. (2016) developed a process that combined ambient noise tomography (ANT) with the WGM to jointly obtain dispersion curves with long period widths and the 3D velocity of the lithosphere beneath the United States.

In 2020, the WGM was applied to earthquakes from different directions to find azimuthal anisotropy for various periods (Cao FH et al., 2020). Cao FH et al. (2023) further jointly inverted the ambient noise, receiver function

and wavefield gradient to obtain the 3D velocity model and azimuthal anisotropy structure.

3. Theoretical framework of the WGM

The core components of the WGM are spatial wavefield gradients (Langston, 2007a). As shown in Figure 2, many factors can contribute to the subtle differences between waveforms observed at two stations, thereby affecting the spatial wavefield gradients. The velocity in the vicinity of the sub-array and wave propagation direction can affect the alignment of the two waveforms, resulting in waveform differences. The geometrical spreading and radiation pattern can affect the relative wave amplitudes with respect to the sub-array geometry and the azimuths of the rays. Thus, the WGM utilizes subtle wavefield differences (i.e., spatial wavefield gradients) to extract the major wave propagation parameters: phase velocity, wave propagation direction, geometrical spreading, and radiation pattern. The variable phase velocity by azimuth can be further used to obtain the azimuthal anisotropy (Cao FH et al., 2020). The differences between the phase velocities of the radial/vertical and transverse components can be used to obtain the radial anisotropy, and the amplitude variation parameters can be used to obtain the attenuation.

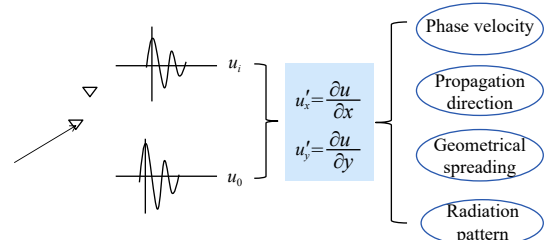


Figure 2. Wavefield gradients and related wave propagation parameters. u_0 is the waveform in reference location, u_i is the waveforms in supporting stations. u'_x and u'_y represent spatial gradients of the wavefield u .

3.1. Spatial wavefield gradients

The spatial gradients of a wavefield are directly related to the wave amplitude and its time derivative (Langston, 2007a). Considering a simple case, the 1D homogeneous wave equation for an isotropic elastic medium is:

$$\frac{1}{c^2} \frac{\partial^2 u}{\partial t^2} - \frac{\partial^2 u}{\partial r^2} = \left(\frac{1}{c} \frac{\partial}{\partial t} - \frac{\partial}{\partial r} \right) \left(\frac{1}{c} \frac{\partial}{\partial t} + \frac{\partial}{\partial r} \right) u = 0, \quad (3-1)$$

where u , c and r are wavefields (displacement, velocity, or acceleration) that are functions of time and location, phase

velocity, and the coordinate along the propagation direction, respectively. The phase velocity c can be obtained directly by finding the second-order temporal and spatial derivatives of the wavefield. This simple form of the WGM was applied to obtain the Rayleigh wave phase velocity directly from ambient noise field (De Ridder and Biondi, 2015).

Assuming that the phase velocity c is constant within a sub-array (a small region), then the wave equation (Equation 3.1) can be reduced to:

$$\frac{1}{c} \frac{\partial u}{\partial t} + \frac{\partial u}{\partial r} = 0, \quad (3-2)$$

which is the second part of the middle term in Equation (3.1) and represents the wave propagating in the positive direction. Therefore, the terms in the middle of Equation (3.1) represent waves propagating in two directions (e.g., Whitham, 1999). Thus, the first-order spatial and temporal gradients of the waveform can be used to obtain the phase velocity of the wave and the properties of the medium.

For a plane wave propagating in the positive direction in a sub-array, the wavefield obeys the wave equation as follows:

$$u(t, r) = f[t - p_r(r - r_0)] \quad (3-3)$$

where f is the function representing a seismic wavefield that varies with distance and time and $p_r = 1/c$ is the slowness. By assuming that the wave amplitude changes as a function of distance r is $G(r)$, then the wave model becomes (Langston, 2007a):

$$u(t, r) = G(r) f[t - p_r(r - r_0)] \quad (3-4)$$

Taking the spatial derivative of the wavefield gives:

$$\frac{\partial u}{\partial r} = A_r u + B_r \frac{\partial u}{\partial t}, \quad (3-5)$$

where

$$A_r = \frac{\partial G(r)}{\partial r} \frac{1}{G(r)}, \quad (3-6)$$

$$B_r = -p_r, \quad (3-7)$$

where A_r is the normalized amplitude gradient (called geometrical spreading in early publications) and B_r is the negative of the radial slowness. Note that p_r is assumed to be constant for a small area.

The wave model (3.4) is sufficient for most cases. However, if the intrinsic attenuation of the medium ($1/Q$) is considered, then the following is obtained:

$$u(t, r) = G_0(r) \exp\left(\frac{-\omega r}{2cQ}\right) f(t - p_r(r - r_0)), \quad (3-8)$$

where $G_0(r)$ represents the wave amplitude varying with distance due to geometrical spreading, ω represents the

angular frequency, and Q represents the quality factor.

Taking the spatial derivative of the wavefield [Equation (3.8)] yields an equation similar to Equation (3.5), but A_r is modified as follows:

$$A_r = \frac{\partial G_0(r)}{\partial r} \frac{1}{G_0(r)} - \frac{\omega}{2cQ} \quad (3-9)$$

In this equation, if the geometry of the array and the source location are known, the geometrical spreading (first term on the right side) can be computed. Therefore, if A_r , c , and ω are known, Q can be estimated.

For a wave propagating in a 2D space, Equation (3-4) can be rewritten as

$$u(t, x, y) = G(x, y) f(t - p_x(x - x_0) - p_y(y - y_0)), \quad (3-10)$$

and the spatial gradients are:

$$\frac{\partial u(t, x, y)}{\partial x} = A_x(x) u(t, x, y) + B_x(x) \frac{\partial u(t, x, y)}{\partial t}, \quad (3-11)$$

$$\frac{\partial u(t, x, y)}{\partial y} = A_y(y) u(t, x, y) + B_y(y) \frac{\partial u(t, x, y)}{\partial t}, \quad (3-12)$$

$$A_x(x) = \frac{1}{G(x, y)} \frac{\partial G(x, y)}{\partial x}, \quad (3-13)$$

$$A_y(y) = \frac{1}{G(x, y)} \frac{\partial G(x, y)}{\partial y}, \quad (3-14)$$

$$B_x(x) = -p_x, \quad (3-15)$$

$$B_y(y) = -p_y, \quad (3-16)$$

where A_x and A_y are the normalized amplitude gradients in the x and y directions, respectively. Here, it is assumed that p_x and p_y are constant in a small array.

Based on the relationship between the Cartesian and cylindrical coordinates ($x = r \sin \theta; y = r \cos \theta$), the following relationships can be obtained:

$$p_r = p_x \sin \theta + p_y \cos \theta, \quad (3-17)$$

$$c = (p_x^2 + p_y^2)^{-\frac{1}{2}}, \quad (3-18)$$

$$\theta = \tan^{-1} \frac{p_x}{p_y}, \quad (3-19)$$

$$A_r(r) = A_x(x) \sin \theta + A_y(y) \cos \theta, \quad (3-20)$$

$$A_\theta = r(A_x(x) \cos(\theta) - A_y(y) \sin(\theta)), \quad (3-21)$$

where p_r , c , θ , A_r , A_θ are slowness, phase velocity, wave propagation direction, geometrical spreading, and radiation pattern, respectively (note: A_r and A_θ are the normalized amplitude gradients). Equations (3.11–3.21) are the fundamental formulas used in the WGM. A workflow is summarized in section 3.4, and the technical details of computing the spatial gradients and WGM parameters A and B are presented in sections 3.2 and 3.3, respectively.

3.2. Computing the wavefield gradients

In the WGM, the first and most important step is to find the spatial wavefield gradients. Spatial gradients $\partial u / \partial x$ and $\partial u / \partial y$ can be measured directly by strain meters. For a seismic array with a regular geometry, a finite-difference method can be applied to compute the spatial gradients (Langston, 2007a). Liang CT and Langston (2009) proposed a weighted inversion method to compute wavefield gradients in an array with an arbitrary geometry. Liu YY and Holt (2015) used a cubic spline interpolation method to obtain a regularly gridded wavefield before applying the finite-difference method to determine the spatial gradients. Maeda et al. (2016) proposed a wavefield gridding method based on first order Taylor series expansion to simultaneously obtain the gridded wavefield and spatial gradients.

3.2.1 Weighted inversion method

Considering the irregular geometry of the USArray, Liang CT and Langston (2009) considered a sub-array (Figure 3). This assumes that the wave functions at receiver $s_i (i = 0, 1, 2, \dots, N)$ are u_i , respectively.

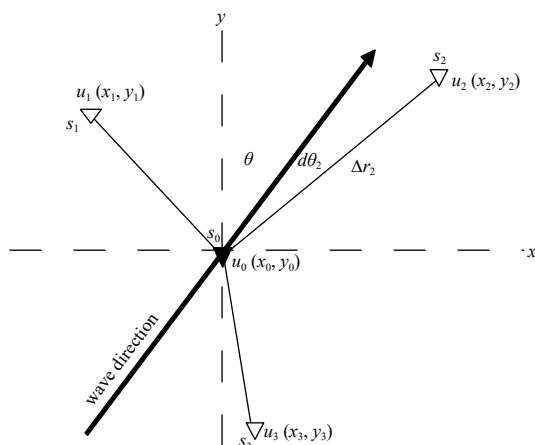


Figure 3. Geometry of an irregular sub-array. To determine the spatial gradients of the primary receiver s_0 , at least three more auxiliary receivers (s_1, s_2, s_3) are required. Here θ and $d\theta_2$ are the azimuth of the ray and the angle between the raypath and the line connecting receiver 2 and the master receiver, respectively. (modified from Figure 2 in Liang CT and Langston, 2009).

Based on the Taylor series, the spatial gradients at the primary receiver s_0 can be related to the wave functions at all other receivers (auxiliary receivers) as follows:

$$u_i - u_0 = \frac{\partial u}{\partial x} \delta x + \frac{\partial u}{\partial y} \delta y + du_i^{\text{err}}, \quad (3-22)$$

where $\delta x = x_i - x_0$ and $\delta y = y_i - y_0$ are the distances between stations s_i and s_0 . The truncation error du_i^{err} has the form:

$$du_i^{\text{err}} <= \delta x_i^2 \frac{\partial u^2}{\partial^2 x}|_{s_0} + \delta y_i^2 \frac{\partial u^2}{\partial^2 y}|_{s_0} + \delta x \delta y \frac{\partial u^2}{\partial x \partial y}|_{s_0}. \quad (3-23)$$

By taking the first order approximation, Equation (3.22) can be written in matrix form as

$$\begin{bmatrix} u_1 - u_0 \\ u_2 - u_0 \\ \vdots \\ u_N - u_0 \end{bmatrix} = \begin{bmatrix} \delta x_1 & \delta y_1 \\ \delta x_2 & \delta y_2 \\ \vdots & \vdots \\ \delta x_N & \delta y_N \end{bmatrix} \begin{bmatrix} \partial u / \partial x \\ \partial u / \partial y \end{bmatrix}. \quad (3-24)$$

Considering the truncation errors, a weighting matrix W can be left-multiplied to both sides of Equation (3-24):

$$W = \begin{bmatrix} w_1 & & & \\ & w_2 & & \\ & & \ddots & \\ & & & w_N \end{bmatrix}. \quad (3-25)$$

The weighting parameters are based on truncation errors and are discussed in detail in Liang CT and Langston (2009). By solving the weighted version of Equation (3.24), the spatial gradients can then be obtained.

3.2.2 Wavefield gridding method

Maeda et al. (2016) proposed an alternative wavefield gridding method. As shown in Figure 4, the study region is divided into grids with uniform spacing. The waveform u_i observed at station S_i can be expressed as:

$$u_i = u_G + \frac{\partial u}{\partial x} (x_i - x_G) + \frac{\partial u}{\partial y} (y_i - y_G) + du_i^{\text{err}}, \quad (3-26)$$

where u_G are the wavefields in the nearby grids. Assuming that N receivers surround the grid, then a matrix [Equation (3.27)] can be obtained:

$$\begin{bmatrix} u_1 \\ u_2 \\ \vdots \\ u_N \end{bmatrix} = \begin{bmatrix} 1 & \delta x_1 & \delta y_1 \\ 1 & \delta x_2 & \delta y_2 \\ \vdots & \vdots & \vdots \\ 1 & \delta x_N & \delta y_N \end{bmatrix} \begin{bmatrix} u_G \\ \partial u / \partial x \\ \partial u / \partial y \end{bmatrix}, \quad (3-27)$$

where δx_i and δy_i are the distances between the grid and the i -th supporting receiver (black triangles in Figure 4a) in the x and y directions, respectively.

Similarly, a weighting matrix can be applied. By solving Equation (3-27), the wavefield and wavefield gradients in a regular grid can be computed simultaneously. Figure 4 shows an example of this process, in which the waveforms at neighboring stations are used to form the left-hand side of Equation (3-27). Note that Equation (3-27) is applicable to a single point in time. After solving the equations for all time points, the interpolated waveform is obtained (red waveform in Figure 4b). Using this process, the waveforms and spatial gradients in all grids can be computed.

3.3. Computing WGM parameters A and B

A_x , A_y , B_x , and B_y are the middle products of the WGM. Three different methods can be used to compute these parameters: the frequency domain (Langston, 2007b), Hilbert transform (Langston, 2007c), and linear

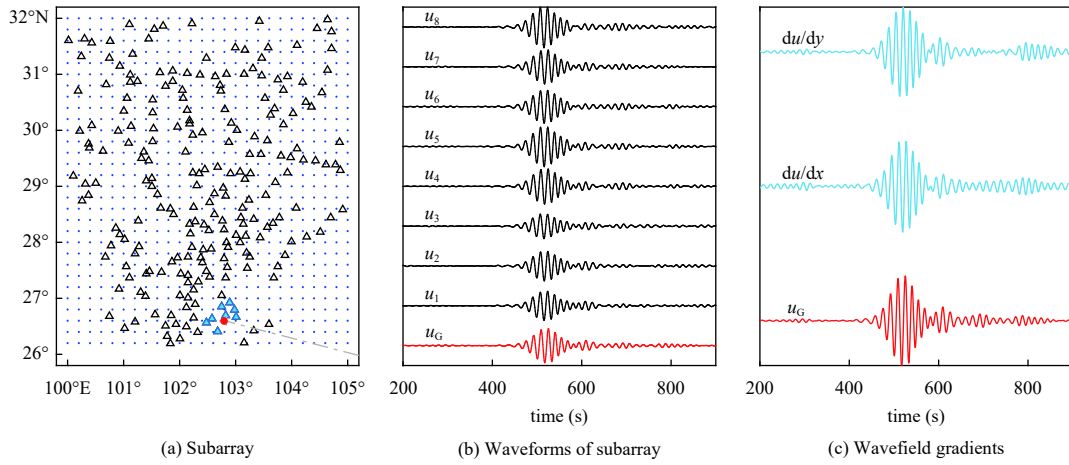


Figure 4. WGM-based wavefield gridding method. (a) Geometry of a subarray. Black triangles and blue dots represent the stations of Chuanxi Array and Grid reference locations, respectively. Blue triangles are the supporting stations of the reference location of red dot, and gray dash line presents the raypath. (b) Red and black waveforms with bandpass filtered (12–18 s) are the reconstructed waveform (u_G) at the reference location and the waveforms of supporting stations ($u_{i=1,2,3,\dots}$), respectively. (c) Red and blue traces are the reconstructed waveform (u_G) and wavefield gradients ($\partial u/\partial x, \partial u/\partial y$) at the reference location.

inversion (Liu YY and Holt, 2015) methods.

3.3.1 Frequency domain method

A Fourier transform is applied to every term in Equations (3-11) and (3-12), and both sides are divided by the Fourier transform of the original waveform, which yields

$$\frac{\partial \widehat{u}(\omega, x, y)}{\partial x}/\widehat{u}(\omega, x, y) = A_x(x) + i\omega B_x(x), \quad (3-28)$$

$$\frac{\partial \widehat{u}(\omega, x, y)}{\partial y}/\widehat{u}(\omega, x, y) = A_y(x) + i\omega B_y(x), \quad (3-29)$$

where \widehat{u} represents the Fourier transform of the original waveform. By identifying the real and imaginary terms on the left sides of Equations (3-28) and (3-29), the following equations are obtained:

$$A_x(x) = \text{real}\{\frac{\partial \widehat{u}(\omega, x, y)}{\partial x}/\widehat{u}(\omega, x, y)\}, \quad (3-30)$$

$$A_y(x) = \text{real}\{\frac{\partial \widehat{u}(\omega, x, y)}{\partial y}/\widehat{u}(\omega, x, y)\} \quad (3-31)$$

$$B_x(x) = \text{im}\{\frac{\partial \widehat{u}(\omega, x, y)}{\partial x}/\widehat{u}(\omega, x, y)\}, \quad (3-32)$$

$$B_y(x) = \text{im}\{\frac{\partial \widehat{u}(\omega, x, y)}{\partial y}/\widehat{u}(\omega, x, y)\}, \quad (3-33)$$

The frequency domain method is simple and easily implemented; however, it can be very unstable for frequencies with a very small or zero spectrum, which is a major drawback.

3.3.2 Hilbert transform method

Langston (2007c) proposed a more accurate and stable method (comparing to the frequency domain method) in time domain, which base on the Hilbert transform of

Equations (3-11) and (3-12):

$$H\left[\frac{\partial u}{\partial x}\right] = A_x H[u] + B_x \frac{\partial}{\partial t} H[u], \quad (3-34)$$

$$H\left[\frac{\partial u}{\partial y}\right] = A_y H[u] + B_y \frac{\partial}{\partial t} H[u], \quad (3-35)$$

where $U_{,j} = H[\partial u/\partial j]$, ($j = x, y$) and $U = H[u]$ are the Hilbert transforms of $\partial u/\partial j$ and u , respectively; $|U_{,j}|$ and $|U|$ are the envelopes or instantaneous amplitudes of $U_{,j}$ and U , respectively; ψ and φ are the phase terms of $U_{,j}$ and U , respectively. Then

$$|U_{,x}| e^{i\psi} = A_x |U| e^{i\varphi} + B_x \frac{\partial}{\partial t} \{|U| e^{i\varphi}\}, \quad (3-36)$$

$$|U_{,y}| e^{i\psi} = A_y |U| e^{i\varphi} + B_y \frac{\partial}{\partial t} \{|U| e^{i\varphi}\}, \quad (3-37)$$

when $\omega(t) = \frac{d\varphi(t)}{dt}$ is set as the instantaneous frequency, the following equations are obtained:

$$B_x = \frac{1}{\omega(t)} \frac{|U_{,x}|}{|U|} \sin(\psi - \varphi), \quad (3-38)$$

$$B_y = \frac{1}{\omega(t)} \frac{|U_{,y}|}{|U|} \sin(\psi - \varphi), \quad (3-39)$$

$$A_x = \frac{|U_{,x}|}{|U|} \cos(\psi - \varphi) - \frac{1}{\omega(t)} \frac{|U_{,x}|}{|U|^2} \frac{\partial |U|}{\partial t} \sin(\psi - \varphi) \quad (3-40)$$

$$A_y = \frac{|U_{,y}|}{|U|} \cos(\psi - \varphi) - \frac{1}{\omega(t)} \frac{|U_{,y}|}{|U|^2} \frac{\partial |U|}{\partial t} \sin(\psi - \varphi) \quad (3-41)$$

where

$$\left\{ \begin{array}{l} U_{,x} = \frac{\partial u}{\partial x} - iH \left[\frac{\partial u}{\partial x} \right] \\ U_{,y} = \frac{\partial u}{\partial y} - iH \left[\frac{\partial u}{\partial y} \right] \\ U = u - iH[u] \\ U_{,t} = \frac{\partial |U|}{\partial t} = \frac{\partial u}{\partial t} - iH \left[\frac{\partial u}{\partial t} \right] \\ \varphi(t) = \tan^{-1} \left[\frac{-H[u(t)]}{u(t)} \right] \\ \psi_j(t) = \tan^{-1} \left[\frac{-H \left[\frac{\partial u}{\partial j}(t) \right]}{\frac{\partial u}{\partial j}(t)} \right], j = x, y \\ \omega(t) = \frac{1}{|U|^2} \left\{ \frac{\partial u}{\partial t} H[u(t)] - u(t) H \left[\frac{\partial u}{\partial t} \right] \right\} \end{array} \right. . \quad (3-42)$$

3.3.3 Time domain linear inversion method

Liu YY and Holt (2015) proposed a linear inversion method to directly invert A_x , A_y , B_x and B_y based on Equations 3.11 and 3.12. The matrix equation is as follows:

$$\left[\begin{array}{cccc} u(t_1) & \dot{u}(t_1) & 0 & 0 \\ 0 & 0 & u(t_1) & u(t_1) \\ \vdots & \vdots & \vdots & \vdots \\ u(t_N) & \dot{u}(t_N) & 0 & 0 \\ 0 & 0 & u(t_N) & \dot{u}(t_N) \end{array} \right] \left[\begin{array}{c} A_x \\ B_x \\ A_y \\ B_y \end{array} \right] = \left[\begin{array}{c} \frac{\partial u}{\partial x}(t_1) \\ \frac{\partial u}{\partial y}(t_1) \\ \vdots \\ \frac{\partial u}{\partial x}(t_N) \\ \frac{\partial u}{\partial y}(t_N) \end{array} \right], \quad (3-43)$$

where $u(t_i)$, $\dot{u}(t_i)$ and $u_{,x}(t_i)$ are the waveform, its time derivative, and its spatial derivative at time t_i , respectively.

This method assumes that all four parameters are constant in the time window $[t_1 \dots t_N]$. This is usually true around the surface wave envelope peak time. However, this assumption may not always be true, particularly at the wave interface times of multiple phases. We believe the Hilbert transform method is currently the most stable and accurate method available.

3.4. Workflow for WGM imaging

Figure 5 shows the major steps involved when the WGM is used for imaging purposes. For a regional seismic

array, after obtaining the original waveforms, the general pre-processing steps include (Liang CT and Langston, 2009): (1) inspecting the data to ensure that the target phases are clean and strong for all receivers; (2) removing instrument responses, wave trends, and means; (3) filtering waveforms to the target frequency bands; (4) removing waveforms that have peak amplitudes $\sim 30\%$ larger or smaller than the peak amplitude of waveform in reference location (Liang CT and Langston, 2009) or the median peak amplitudes of the waveforms in the same sub-array (Cao FH et al., 2023); and (5) applying the reducing velocity method by shifting the waveforms according to an average phase velocity (e.g., 4 km/s) to remove the effects of the background velocity. Thus, the computed phase velocity represents a perturbation with respect to the average velocity c . The spatial wavefield gradients are then computed using either the weighted inversion [Equation (3-27)] or linear wavefield gridding [Equation (3-24)] method.

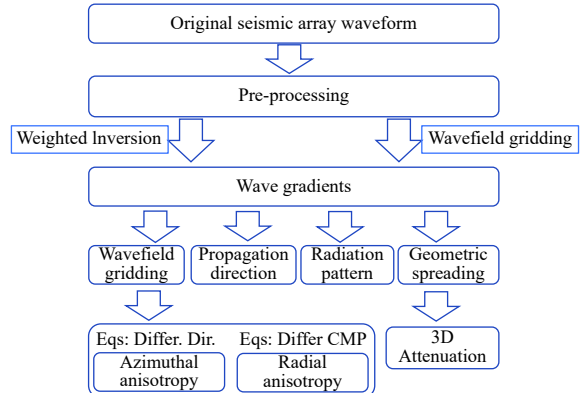


Figure 5. Workflow of the WGM. Eqs: Differ. Dir.: Using earthquakes from different directions. Differ. CMP: different components.

After obtaining the spatial gradients, A_x , A_y , B_x , and B_y can be computed using one of the three methods described in section 3.3 using either of the frequency domain methods [Equations (3.30–3.33)], the Hilbert transform method [Equations (3.38–3.41)], or the linear inversion method [Equation (3-43)]. The four parameters are then substituted into Equations (3.18–3.21) to obtain the phase velocity, wave direction, geometrical spreading, and radiation pattern. By accounting for the average velocity c , the true slowness can be obtained using $p_x = p'_x + \frac{\sin\theta}{\bar{c}}$, and $p_y = p'_y + \frac{\cos\theta}{\bar{c}}$, where p'_x and p'_y are the slowness values computed using a reducing velocity, \bar{c} is the initial average velocity, and θ is the wave propagation direction.

All of the parameters are a function of time. Technically, the WGM can be applied to any phase with high signal-noise ratio (SNR>5). The surface wave energy

is often the strongest on a waveform, particularly for teleseismic data; therefore, many WGM applications are based on surface waves. For surface waves, the phase velocity and other parameters are selected at the time corresponding to the envelope peak. The phase velocity at the peak time is then used as the reduced velocity and the process is repeated from step (5) until the phase velocity difference between two successive loops is less than 0.01 km/s. In practice, ~3 loops are usually required to reach this threshold.

The four parameters are the only middle products that can be processed further to obtain the properties of the medium. For example, by processing waveforms from different directions, phase velocity as it varies with azimuth can be obtained, as well as the azimuthal anisotropy. By working on three components of the waveforms, phase velocities of Rayleigh and Love wave can be obtained for the inversion of shear wave velocity in horizontal and vertical polarization, and then radial anisotropy can be computed. Based on the normalized amplitude gradient (A_r), attenuation can also be obtained.

Currently, WGM is commonly used to compute 3D velocities and anisotropy.

4. WGM applications

Since its introduction to seismology, the WGM has been applied to a wide range of datasets for different purposes. The major applications are summarized in [Table 1](#) and their timeline is shown in [Figure 6](#). Theoretically, the WGM can be applied to the full waveform to obtain the major WGM attributes (i.e., phase velocity, wave propagation direction, geometrical spreading, and radiation patterns). However, each study may have a different focus. As shown in [Table 1](#), the applications can be divided into 4 categories based on the target data type. Full waveforms were analyzed in six studies, ambient noise data was used in four studies to extract phase velocities and anisotropy, and body waves were the focus of four studies. However, most studies were concentrated on surface waves owing to their strong energy. The arrays used for data collection

Table 1. Major applications of the WGM in previous studies.

Data Type	Application	Array	Major Results
Full waveform	Langston et al., 2007a, c	1D $N_s = 8, dx = 15m$	Proposed the WGM and time/frequency domain methods to compute A and B parameters. Obtained slowness and geometrical spreading along the ray path.
Full waveform	Langston et al., 2007b	2D $dx = 10\text{--}20 km$	Proposed 2D WGM to compute the 4 WGM attributes: phase velocity, wave direction, geometrical spreading, and radiation pattern.
Full waveform	Langston and Liang CT, 2008	2D ANZA Array $dx = 10 km$	Used 2D array to compute rotational components of the wave field.
Full waveform	Barker and Langston, 2016	1D+2D $N_s=24$ $dx = 2 m$	Used 1D array and 2D gradiometer to test the WGM's performance on phase separation and source location, etc.
Full waveform	Maeda et al., 2016	2D Hinet (Japan)	Proposed the wavefield gridding method to extract spatial gradients
Full waveform	Challu et al., 2021	2D $N_s=4 \times 4,$ $dx = 5 m$	Used the WGM attributes with AI techniques to distinguish explosions from earthquakes.
Ambient noise field	De Ridder and Biondi, 2015; De Ridder and Curtis, 2017	2D, Ocean Bottom Cable, Inline $dx = 50m$ Crossline $dx = 300 m$	Used second order derivatives of the noise wavefield to find phase velocity and anisotropy based on the Helmholtz equation.
Noise field	Cao RK et al., 2020	2D 8×11 array $dx = 5 m$	Similar to Ridder and Curtis (2017), but further inverted phase velocity dispersion to obtain a 3D velocity model.
Noise field	Edme and Yuan SH, 2016	2D, 3 sub-arrays, each with 3 seismometers, $dx = 1.5\text{--}3 m$	Used three 3-station wave gradiometers to measure wavefield gradients, from which the dispersion curve and wave direction were obtained.

Continued

Data Type	Application	Array	Major Results
Body waves	Langston and Ayele, 2016	1D Vertical well	Obtained impedance and attenuation profiles in the SAFOD well.
Body waves	Sollberger et al., 2016	2D Moon Array $N_s=4$	Used WGM to obtain phase velocity, rotational ground motion, propagation direction, and shear wave arrivals, which were inverted to obtain the surface structure of the Moon.
Body waves	Van Renterghem et al., 2018	1D Length = 250 m $dx = 1.5\text{m}$	Used spatial gradients to obtain phase velocities, which were then used to obtain the horizontal wavenumber .
Surface waves	Liang CT and Langston, 2009	2D USArray $dx = 70\text{ km}$	Proposed linear inversion method to obtain spatial gradients.
Surface waves	Poppeliers, 2011	2D Glendora Array $dx = 3\text{ m}$ $N_s=13$	Used wavelet transform in the WGM.
Surface waves	Liu YY and Holt, 2015	2D USArray $dx = 70\text{ km}$	Developed velocity correction based on the Helmholtz equation.
Surface waves	Porter et al., 2016	2D USArray $dx = 70\text{ km}$	Combined noise+WGM to obtain 3D velocities beneath the continental US (0–150 km).
Surface waves	Zhou L et al., 2017	2D USArray $dx = 70\text{ km}$	Used three components to obtain SH and SV velocities.
Surface waves	Cao FH et al., 2020	2D ChinArray $dx = 20\text{--}35\text{ km}$ $N_s = 303$	Obtained azimuthal anisotropy for different periods.
Surface waves	Cao FH et al., 2023	2D ChinArray $dx = 20\text{--}35\text{ km}$ $N_s = 303$	Combined noise+WGM+receiver function to obtain 3D velocity and anisotropy at 0–100 km depth.
Surface waves	Chang YN et al., 2022	2D, Local; $dx = 6.5\text{ km};$ $N_s = 163$	Obtained 3D v_S at 0–20 km depth and for a grid spacing of 5 km.

Note: dx =station spacing; N_s =number of stations

varied widely in scale (i.e., from a few meter to thousands of kilometer) and in their average station spacing (1 m–70 km). The frequency bands of the waves varied from 100 Hz to 150 s, which was highly dependent on the geometry of the array.

4.1. WGM application to full waveforms

The WGM is applicable to the full waveform. The first few studies by Langston et al. were based on the full waveform (sections 4.1.1 and 4.1.2). In addition, Maeda et al. (2016) proposed a WGM-based wavefield gridding method (section 3.2.2) to obtain the full wavefield along with the spatial gradients in regular grids. Challu et al. (2021) used the WGM to process full waveforms along with artificial intelligence methods and to distinguish between explosions and earthquakes. These applications

are representative examples that show the applicability of the WGM to all phases.

4.1.1 WGM attributes for different phases

The first few WGM studies used full waveform analysis to determine the propagation parameters of all phases. For example, the very first study applied the WGM to a linear array to obtain the ray parameter and geometrical spreading as they varied over time (Langston, 2007a). The linear array in the Mississippi (US) embayment consisted of eight strong motion accelerometers with an average spacing of 15 m. The two explosion sources were located 1.3 km and 2.5 km along the receiver line. The original waveforms recorded by the seismometers were corrected for displacement and bandpass filtered (10–15 Hz) before the WGM was applied. Figure 7 shows the overlapping computed ray parameters (background

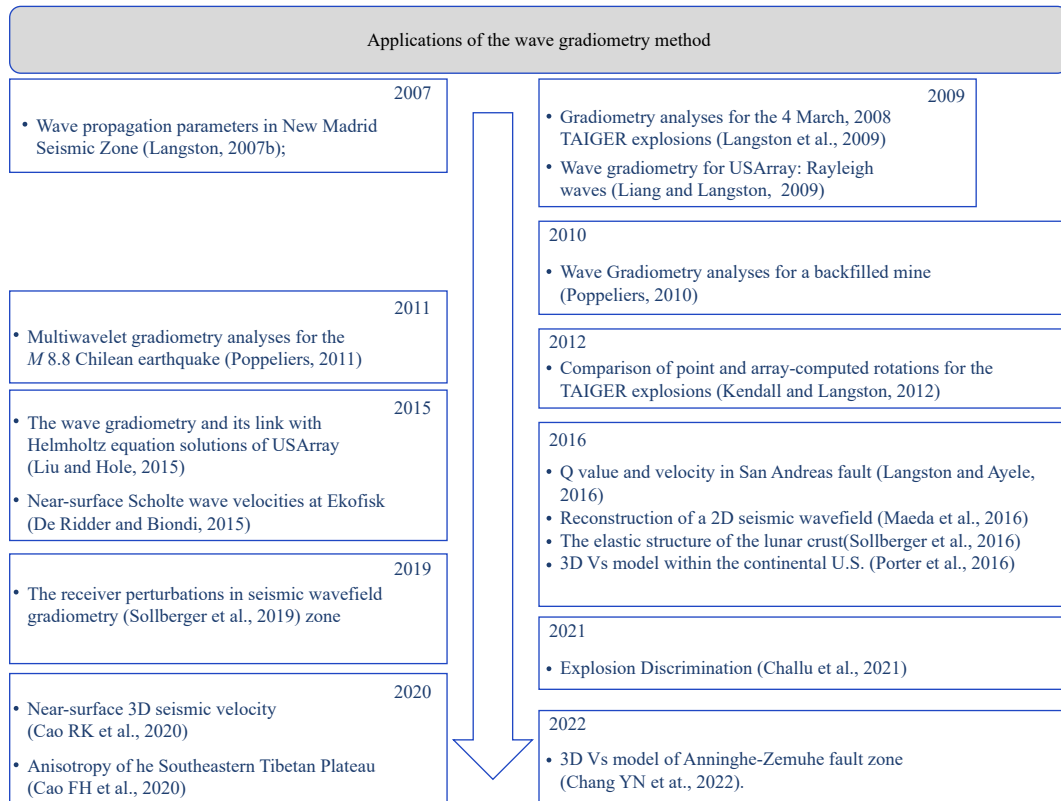


Figure 6. Timeline of major applications of the WGM by previous studies.

color) and waveforms for the central six receivers. The estimated ray parameters were consistent with the waveforms.

Barker and Langston (2016) used a geophone array with a specifically designed gradiometer (Figure 8a) to test the performance of the WGM in a 2D array. In such a small-scale array with a frequency band of 20–115 Hz, the slowness changed substantially. The wave propagation directions are similar to the source-receiver path but still exhibit obvious variations. This may imply that, for a high-frequency band, wave propagation is strongly affected by the structure within and outside the array.

4.1.2 Using the WGM to compute strain and rotation tensors

For a 2D array, the two horizontal component waveforms can be rotated to the x and y directions (u_x and u_y). The spatial derivative of either of the u_x or u_y with respect to x or y can then be obtained. Based on these results, Langston and Liang CT (2008) obtained the second-order strain and rotation tensors (Equations 2.1 and 2.2). Figure 9 shows the doubled shear strain ($u_{1,2} + u_{2,1}$) and rotation ($u_{1,2} - u_{2,1}$). Attributes of P-SV and SH waves, including horizontal slowness and its changes, and changes in geometrical spreading, radiation pattern, propagation azimuth, and wave polarization can be determined by measuring the horizontal strain and rotation of the wavefield along with the three displacement components.

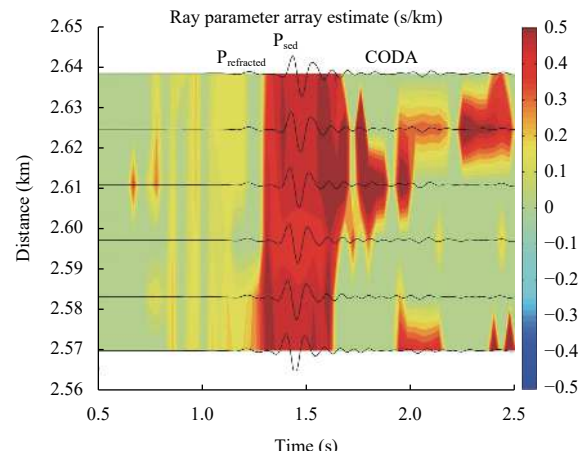


Figure 7. Ray parameters (background color) determined using the WGM were consistent with the major phases. $P_{\text{refracted}}$ and P_{sed} are refracted and sedimentary P waves, respectively (modified from Figure 5 in Langston, 2007a).

Gradiometer cells comprising an array of three-component seismographs can be used to provide estimates of the wavefield gradients.

To compute the third-order strain and rotation tensors (Equations 4.1 and 4.2), the spatial gradients with respect to the z -axis are required; thus, at least two receivers must be located along the z -axis.

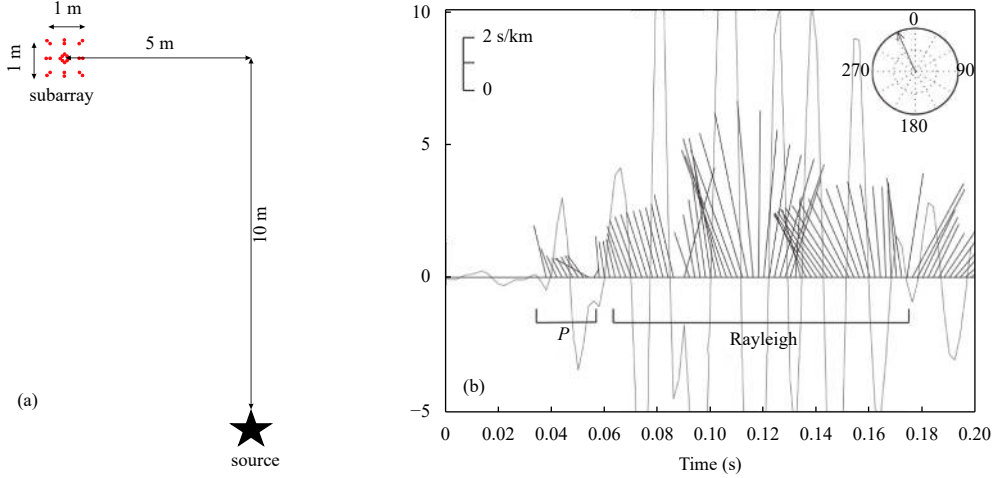


Figure 8. (a) Designed seismic gradiometer. Red dots are seismic sensors, pentagram presents source. (b) Feather plot of the measured wave propagation directions (vector directions) and slowness (vector lengths). The waveform is co-plotted on the central station (gray continuous curve). The upper right inset shows the ray connecting the source and the central receiver in the array (modified from Figure 1 and Figure 7 in Barker and Langston, 2016).

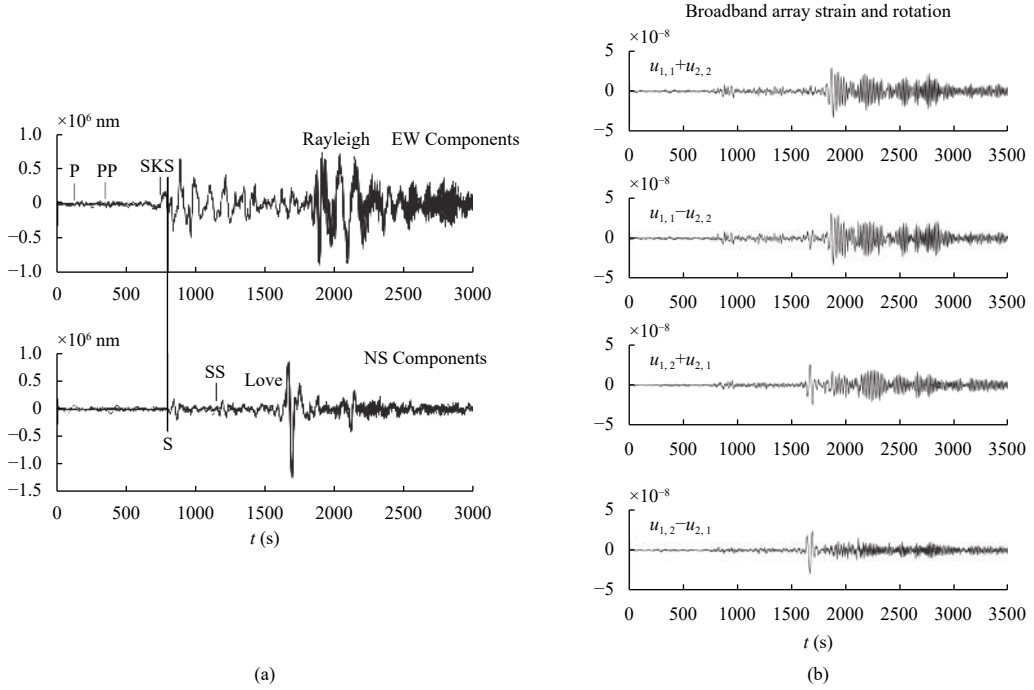


Figure 9. Using two horizontal component waveforms (a) to compute strain and rotation (b). $u_{i,j}$ is the spatial derivative of the i -th component waveform with respect to the j -th axis. Four time series are (from top to bottom): bulk normal strain, differential normal strain, shear strain, and rotation (modified from the Figures 6 and 9 in Langston and Liang CT, 2009).

$$\boldsymbol{\varepsilon} = \begin{pmatrix} \frac{\partial u_x}{\partial x} & \frac{1}{2} \left(\frac{\partial u_x}{\partial y} + \frac{\partial u_y}{\partial x} \right) & \frac{1}{2} \left(\frac{\partial u_x}{\partial z} + \frac{\partial u_z}{\partial x} \right) \\ \frac{1}{2} \left(\frac{\partial u_x}{\partial y} + \frac{\partial u_y}{\partial x} \right) & \frac{\partial u_y}{\partial y} & \frac{1}{2} \left(\frac{\partial u_z}{\partial y} + \frac{\partial u_y}{\partial z} \right) \\ \frac{1}{2} \left(\frac{\partial u_x}{\partial z} + \frac{\partial u_z}{\partial x} \right) & \frac{1}{2} \left(\frac{\partial u_z}{\partial y} + \frac{\partial u_y}{\partial z} \right) & \frac{\partial u_z}{\partial z} \end{pmatrix}, \quad (4-1)$$

$$\boldsymbol{\gamma} = \begin{pmatrix} 0 & \frac{1}{2} \left(\frac{\partial u_x}{\partial y} - \frac{\partial u_y}{\partial x} \right) & \frac{1}{2} \left(\frac{\partial u_x}{\partial z} - \frac{\partial u_z}{\partial x} \right) \\ \frac{1}{2} \left(\frac{\partial u_y}{\partial x} - \frac{\partial u_x}{\partial y} \right) & 0 & \frac{1}{2} \left(\frac{\partial u_y}{\partial z} - \frac{\partial u_z}{\partial y} \right) \\ \frac{1}{2} \left(\frac{\partial u_z}{\partial x} - \frac{\partial u_x}{\partial z} \right) & \frac{1}{2} \left(\frac{\partial u_z}{\partial y} - \frac{\partial u_y}{\partial z} \right) & 0 \end{pmatrix}, \quad (4-2)$$

where $\boldsymbol{\varepsilon}$ and $\boldsymbol{\gamma}$ are the strain and rotation tensors, respectively. At the free surface, if it is assumed that the

traction normal to the surface vanishes, the corresponding shear strain is zero and the normal strain in the z direction can be associated with the normal strain in the other two directions (Spudich et al., 1995; Robertsson and Curtis, 2002), which yields

$$\frac{\partial u_x}{\partial z} = -\frac{\partial u_z}{\partial x}, \quad (4-3)$$

$$\frac{\partial u_y}{\partial z} = -\frac{\partial u_z}{\partial y}, \quad (4-4)$$

$$\frac{\partial u_z}{\partial z} = -\frac{\lambda}{2\mu} \left(\frac{\partial u_x}{\partial x} + \frac{\partial u_y}{\partial y} \right). \quad (4-5)$$

The strain and rotation tensors can then be written as:

$$\boldsymbol{\epsilon} = \begin{pmatrix} \frac{\partial u_x}{\partial x} & \frac{1}{2} \left(\frac{\partial u_x}{\partial y} + \frac{\partial u_y}{\partial x} \right) & 0 \\ \frac{1}{2} \left(\frac{\partial u_x}{\partial y} + \frac{\partial u_y}{\partial x} \right) & \frac{\partial u_y}{\partial y} & 0 \\ 0 & 0 & -\frac{\lambda}{\lambda+2\mu} \left(\frac{\partial u_x}{\partial x} + \frac{\partial u_y}{\partial y} \right) \end{pmatrix}. \quad (4-6)$$

$$\boldsymbol{\gamma} = \begin{pmatrix} 0 & \frac{1}{2} \left(\frac{\partial u_x}{\partial y} - \frac{\partial u_y}{\partial x} \right) & \frac{\partial u_x}{\partial z} \\ \frac{1}{2} \left(\frac{\partial u_y}{\partial x} - \frac{\partial u_x}{\partial y} \right) & 0 & \frac{\partial u_y}{\partial z} \\ -\frac{\partial u_x}{\partial z} & -\frac{\partial u_y}{\partial z} & 0 \end{pmatrix}. \quad (4-7)$$

Therefore, even without the spatial derivative with respect to the z -axis, the strain and rotation tensors can be determined fully when an isotropic medium is assumed.

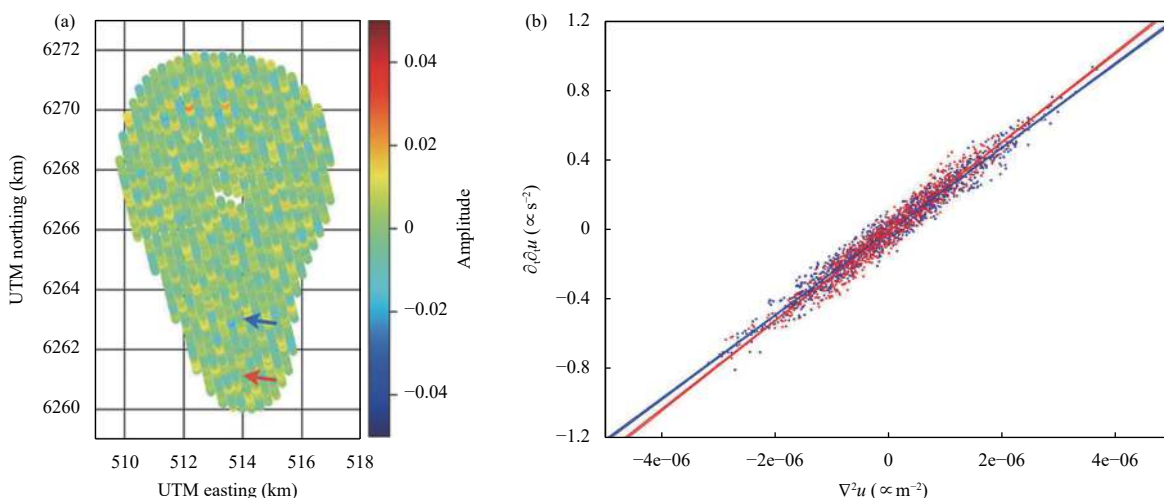


Figure 10. Ambient noise field imaging based on the WGM. (a) Snapshot of seismic noise filtered from 0.6 to 0.8 Hz. (b) Scatterplot of the second-order spatial vs. temporal gradients. Red and blue dots correspond to the two locations marked in Figure 10a (Figure 1 in De Ridder and Biondi, 2015).

Figure 9 shows the ϵ_{33} , ϵ_{12} , γ_{12} , and the different normal strains in time series. γ_{12} represents the rotation around the z -axis.

4.2. WGM application to ambient noise field

The WGM is also applicable to ambient noise fields (De Ridder and Biondi, 2015). The majority of such studies were based on the Helmholtz equation without considering the source term. Referring to Equation 2.3, the second term on the left side is the second temporal derivative. Therefore, the square of the phase velocity can be obtained by linear regression of the second-order spatial and temporal derivatives (Figure 10).

De Ridder and Curtis (2017) used this method to determine the velocity and anisotropy of the same dataset. Cao RK et al. (2020) applied a similar technique to obtain the dispersion curve for each location in a 2D array with a spacing of 5 m and inverted a 3D model for the upper 25 m. Based on the first-order derivative WGM, Edme and Yuan SH (2016) designed a seismometer comprising 3 sensors to obtain the near-surface structure.

4.3. WGM application to body waves

A few studies have focused on body waves. Langston and Ayele (2016) applied the WGM to a vertical array along the SAFOD to obtain the impedance profile and estimate the average attenuation. Sollberger et al. (2016) used spatial gradients to obtain the phase velocity and rotational ground motion, which were used to identify shear wave arrivals on Moonquake waveforms. Van Renterghem et al. (2018) used the WGM to separate

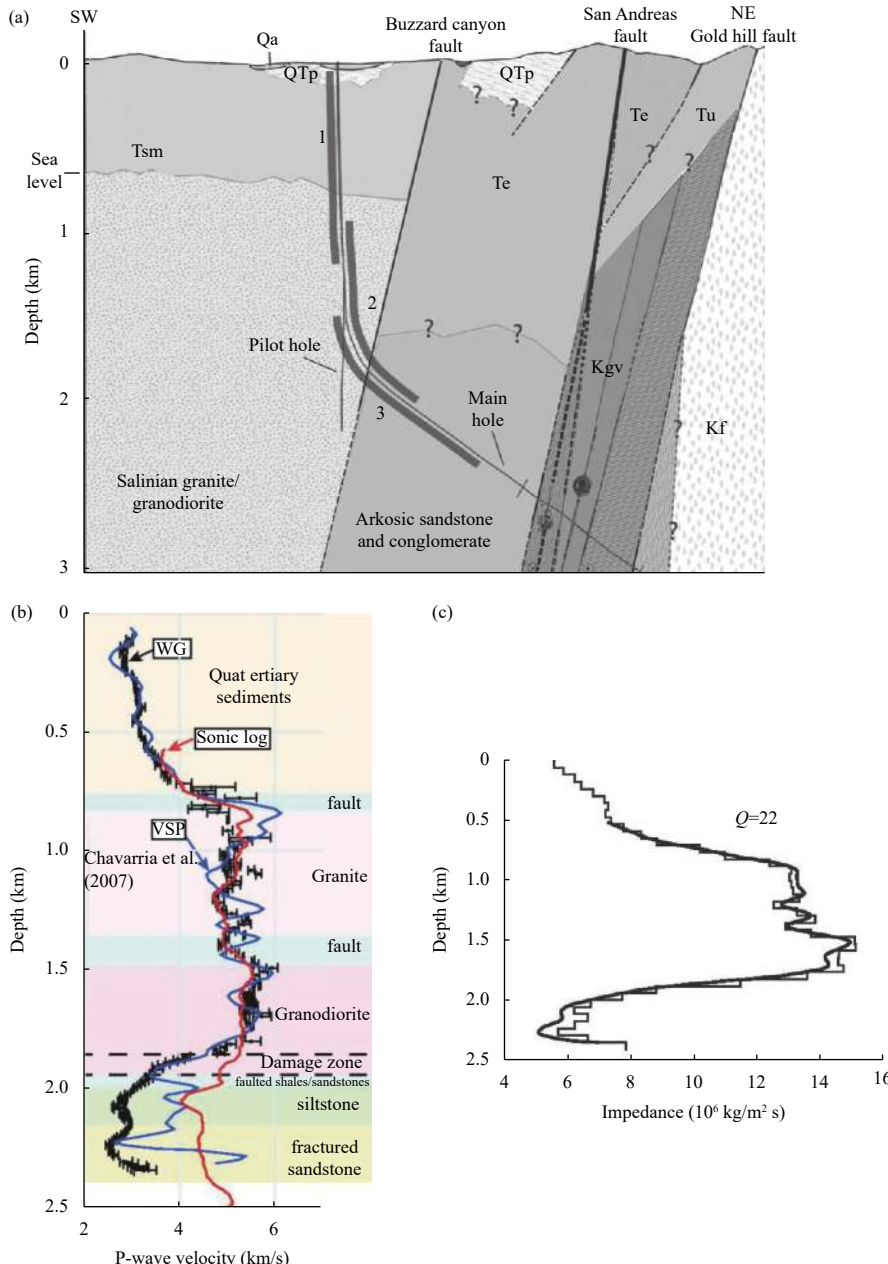


Figure 11. (a) Geometry of the San Andreas Fault Observatory at Depth (SAFOD) well. (b) WGM-estimated P wave velocity (black dots with error bars). Red line: sonic logging with a 75 m moving average; blue line: vertical seismic profiling. (c) Inverted impedance profile with $Q=22$ (modified from the Figures 4 and 6 in Langston et al., 2016).

dowgoing and upgoing body waves.

4.3.1 Computing impedance and attenuation in the SAFOD drilling hole

Langston et al. (2016) used the body waves recorded by the SAFOD seismic array. The main SAFOD hole was drilled to 1.5 km vertically, then continued to a depth of 2.4 km at an angle of $\sim 60^\circ$ from vertical into an actively creeping segment of the San Andreas Fault (Hickman and Zoback, 2004; Zoback et al., 2011). The WGM-determined P wave velocities were generally consistent with the sonic log above 1.6 km (Figure 11b). The inconsistencies

observed below 1.6 km were due to the geometry of the array as it deviated from vertical (Figure 11a).

4.3.2 Identifying Moonquake shear waves

Sollberger et al. (2016) found a special use for the WGM with respect to seismic waveforms on the Moon, or Moonquakes. The Apollo 17 lunar seismic profiling experiment consists of four stations with ~ 60 m spacing. Similar to Langston and Liang CT (2008), they computed the rotation vector based on the WGM to distinguish between P and S waves, which was then used as a tool for picking shear wave arrivals. The basic assumption was that

the shear energy associated with the S wave should be substantially larger than that of the P wave.

For a ground motion rate $\mathbf{v} = \begin{pmatrix} v_x & v_y & v_z \end{pmatrix}$, the rotational ground motion rate is

$$\mathbf{r} = \frac{1}{2} \nabla \times \mathbf{v} = \frac{1}{2} \begin{pmatrix} \partial_y v_z - \partial_z v_y \\ \partial_z v_x - \partial_x v_z \\ \partial_x v_y - \partial_y v_x \end{pmatrix} \quad (4-8)$$

where $\partial_i v_j$ is the spatial derivative of v_j with respect to the i -th axis. However, at the free surface, the traction normal to the surface vanishes, which imposes additional constraints on the vertical derivatives z of the particle velocities (Spudich et al., 1995; Robertsson and Curtis, 2002):

$$\mathbf{r} = \frac{1}{2} \nabla \times \mathbf{v} = \begin{pmatrix} \partial_y v_z \\ -\partial_x v_z \\ \partial_x v_y - \partial_y v_x \end{pmatrix}. \quad (4-9)$$

In Figure 12, the colored background of the center column is the sum of the squares of the two rotational ground motion components around orthogonal horizontal axes (r_x, r_y) obtained from the spatial gradients. As expected, the P wave was associated with minimal rotational energy. The direct S waves had the strongest rotational energy, while the reflected S wave rotational energy was strong enough to identify its phase.

4.4. WGM applications to surface waves

Surface waves are often the strongest in a seismic waveform, particularly for teleseismic waves. Therefore, most applications of the WGM have been based on surface

waves, particularly for regional-scale studies.

4.4.1 Applying the WGM to an irregular regional array

Liang CT and Langston (2009) applied the WGM to the USArray in the western US. This was the first application of the WGM to a regional array to obtain phase velocity maps for periods up to 120 s. They found that the waveform from a single earthquake could be used to obtain the structure beneath a dense array. This makes the WGM superior to other methods when a limited number of seismic sources are available, such as on the Moon.

4.4.2 Combining the WGM and ambient noise tomography to image the lithosphere beneath the US

Liu YY and Holt (2015) applied the WGM to the USArray in the eastern US. They introduced the phase velocity correction term by considering the Helmholtz equation. They also determined the linear relationship between the apparent amplitude decay and the focusing and defocusing effects. Based on this method, Porter et al. (2016) combined the relatively shorter period (8–40 s) dispersion curves from ambient noise cross-correlation with relatively longer period (20–150 s) curves obtained from the WGM (Figure 14). The dispersion curves of the overlapping periods were then averaged over the two datasets. By combining the two datasets, the dispersion curve was extended to cover periods of 8–150 s. Therefore, inversion could image the structure to a depth of 150 km (Figure 15). The results of this study indicated that the major advantage of the WGM is its capability to extract

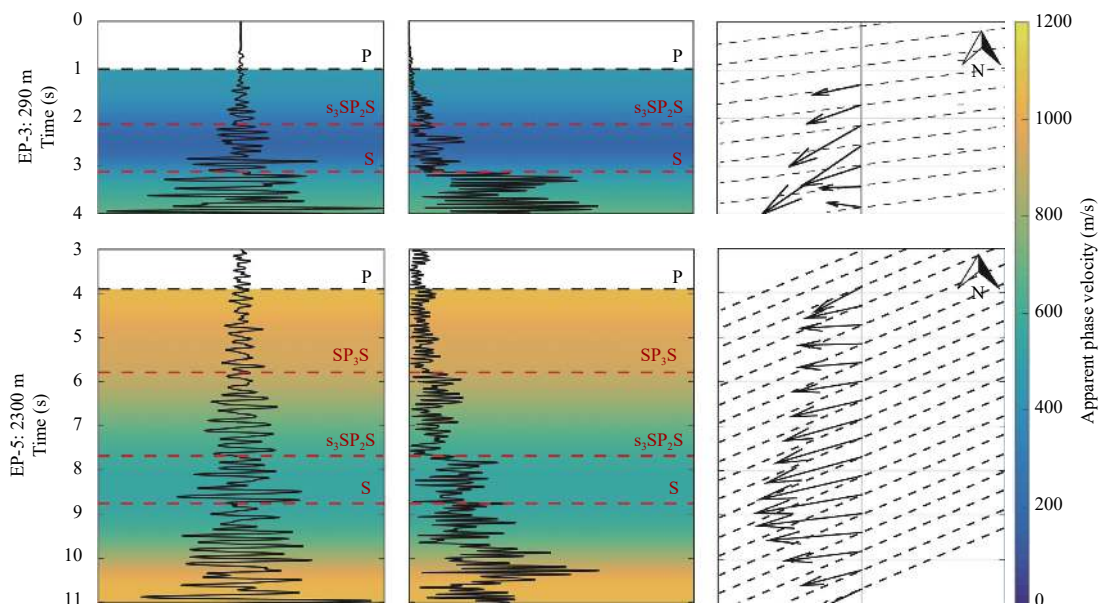


Figure 12. Using the WGM to determine phase velocity (color), rotational ground motion (black curve in the center column), and propagation direction (arrows in the right column). Ray-path directions are shown as dashed lines. The shear waves were identified by the increasing rotational ground motion. The top and lower rows are for events EP-3 and EP-5, respectively (Figure 2 in Sollberger et al., 2016).

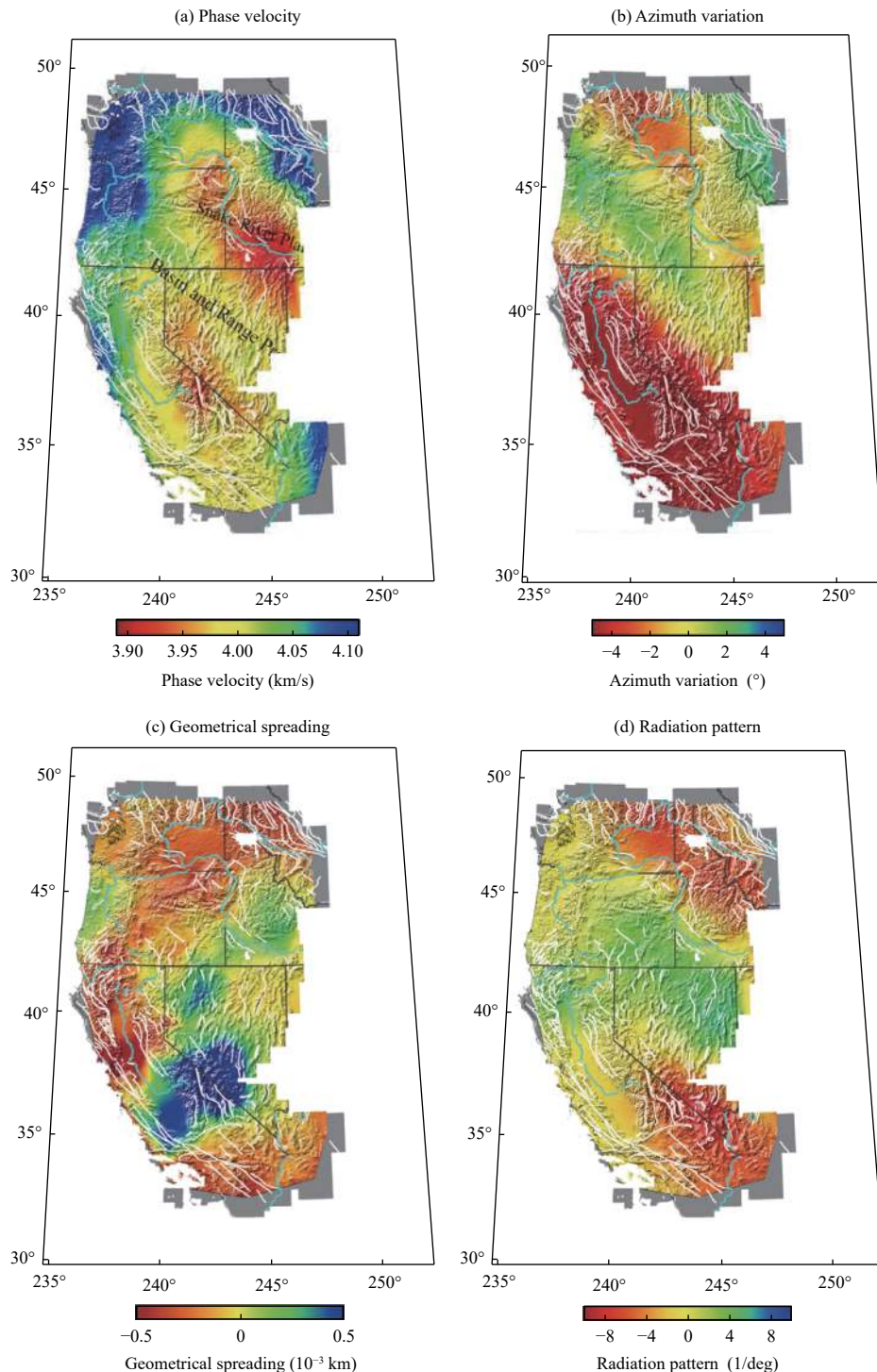


Figure 13. Applying the WGM to the USAArray. The results are based on waveforms from one earthquake in the Kuril Islands (Figure 8 in Liang CT and Langston, 2009). The four major parameters obtained from the WGM are phase velocity (a), azimuth variation (b), geometrical spreading (c), and radiation pattern (d).

much deeper structures than ANT.

4.4.3 Using WGM to invert for 3D velocity and azimuthal anisotropy

Figure 15 shows the capacity of the WGM to invert for 3D velocity structures to a depth of 150 km. Cao FH et al.

(2020) extended the WGM to extract the azimuthal anisotropy based on a regional array. Figure 16 shows the azimuthal anisotropy measurements for sample stations in eight blocks. Using earthquake waveforms from different azimuths, the phase velocities for the different azimuths

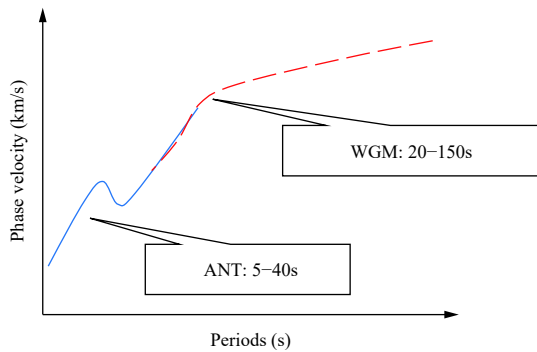


Figure 14. Ambient Noise Tomography (ANT) combined with the WGM to obtain a wide-band dispersion curve. The ANT is often limited to periods less than 40 s owing to the limited frequency of the noise source.

were extracted (colored dots in [Figure 16](#)). The medians of all 18 azimuth windows (black dots in each sub-figure) were modeled as 2nd order sine/cosine functions (red curves) to obtain the anisotropy parameters. The fits were generally good for the majority of the stations. However, for stations such as KLX01, 4th order sine/cosine functions may be necessary to account for back-scattering owing to complex local structures. The same process was applied to all stations.

[Figure 17](#) shows the anisotropy for $T=60$ s. For a single location, an azimuth dependent dispersion curve inversion (ADDCI, [Liang CT et al., 2020](#)) was applied to invert for 3D velocities and azimuthal anisotropy. Cao FH et al. ([2023](#)) combined ANT and WGM to obtain dispersion curves for periods of 5–60 s, and inverted with the receiver functions to obtain the high-resolution 3D v_S model and azimuthal anisotropy structure of the southeastern Tibetan Plateau.

4.4.4 Applying the WGM to a dense, short-period seismic array to image fault zones

[Chang YN et al. \(2022\)](#) applied the WGM to a dense array along the Anninghe-Zemuhe fault. The average spacing of the array was ~ 6.5 km, and the corner frequency of the instruments was ~ 0.2 Hz (10 s). Synthetic tests were conducted to analyze the resolution of the method ([Figure 18](#)). For an array with an average station spacing of ~ 5 km, the WGM is able to resolve a velocity anomaly of ~ 5 km, which is the same as the array's spacing. Data noise may lower the resolution somewhat by smearing the blocking boundary, but the resolution is ~ 1.5 times the array spacing (7.5 km) for noise levels up to 8%.

Finally, the Rayleigh wave phase velocities within period range of 5–15 s were extracted using the WGM, and the 3D S wave velocity structure of the upper crust (3–20 km) along the Anninghe-Zemuhe fault was inverted ([Figure 19](#)). The inversion results were consistent with the

known geological structure, suggesting that the WGM can be used to effectively invert high-resolution 3D velocity structures in a small area. This is particularly useful because an increasing number of short-period instruments are being deployed to monitor seismicity along faults. By applying the WGM, the 3D velocity structure of the upper crust can be obtained, which is almost impossible when using the ANT method (owing to the small scale of the array).

5. Comparisons with other imaging methods

As seismic arrays are used increasingly for subsurface imaging, many techniques have been developed to fully utilize these data. Most recently, ANT, Eikonal tomography, and its cousin Helmholtz tomography are some of the main imaging techniques used in global seismology. [Table 2](#) summarizes these four methods.

5.1. WGM vs. ANT

ANT was introduced by [Campillo and Paul \(2003\)](#) and then used widely at different scales to image the subsurface. ANT starts with finding the empirical Green functions between two stations by cross-correlating the ambient noise at both stations. Because the surface waves dominate the ambient noise field ([Zhang H et al., 2022](#)), the surface waves are often the strongest phases in the empirical Green functions. Therefore, the ANT is reduced to surface wave tomography by directly inverting the empirical surface wave or inverting the dispersion curves of the empirical surface waves. The dispersion curves are often measured using the frequency-time analysis (FTAN) method ([Bensen et al., 2008](#)).

The WGM works on the actual waveform whether it is the ambient noise field or the waveform emitted by an earthquake. For the most common practices, the WGM works on the surface waves emitted by an earthquake. Unlike the ANT, the WGM computes the phase velocity dispersion curves by determining the spatial wavefield gradients.

Although both ANT and the WGM are often reduced to surface dispersion curve inversion, the methods differ in many ways. The working frequency band is the most prominent difference. The empirical Green function is relatively weak for periods longer than 40 s, as it is limited by the frequency band of the ambient noise source. Therefore, ANT is often applicable only for periods less than 40 s. In contrast, the WGM is best suited for long periods. For example, in the USArray, [Porter et al. \(2016\)](#)

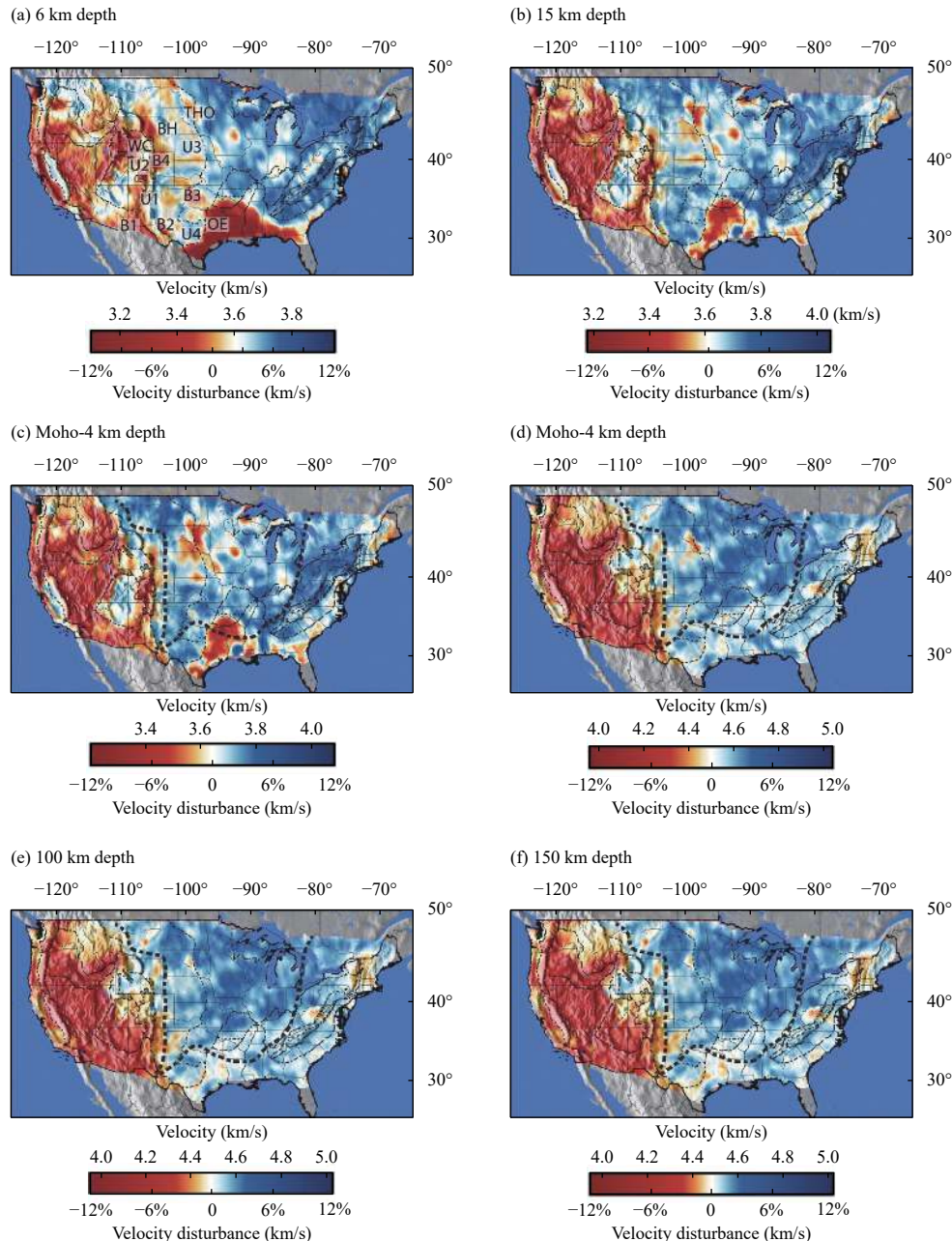


Figure 15. 3D shear wave velocity model of the continental US based on joint inversions of WGM and ANT. The tick labels on the top and bottom of color bars indicate absolute velocity and velocity disturbance, respectively. (Figure 2 in Porter et al., 2016).

extracted dispersion curves with periods of 8–40 s using ANT and 20–150 s using the WGM. Therefore, the ANT is better at extracting surface structures from waves with periods less than 20 s, while the WGM is better at extracting deep structures from waves with periods greater than 40 s. The best practice is to combine the two datasets (Figure 14), as in Porter et al. (2016) and Cao FH et al. (2023).

Both ANT and the WGM work on periods of 20–40 s. Porter et al. (2016) and Cao FH et al. (2023) compared the

phase velocities for the overlapping periods using both methods. As shown in Figures 20 and 21, the phase velocities obtained using ANT and the WGM were remarkably consistent with each other, and the majority of the velocity differences were less than 0.05 km/s. The azimuthal anisotropies of the overlapping periods were also remarkably consistent between methods (Figure 21; Cao FH et al., 2023). These analyses indicate that the WGM works as well as ANT in the frequency band that is applicable to both methods.

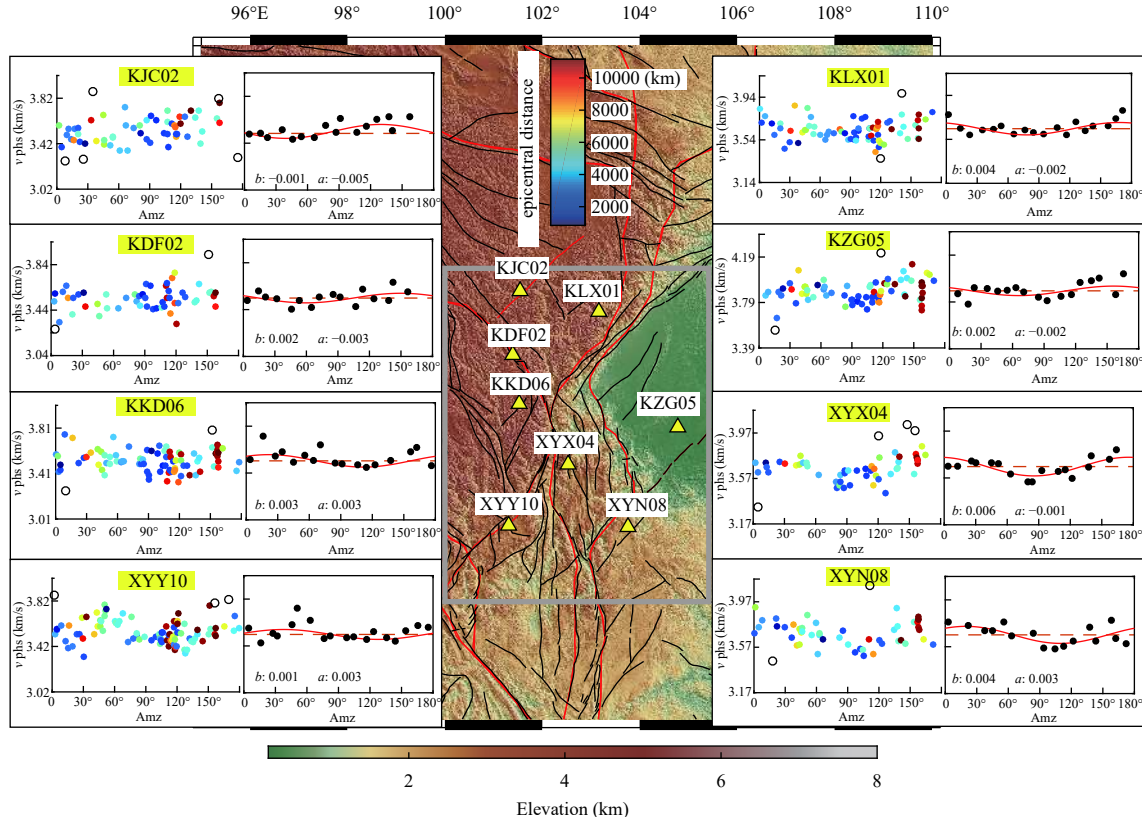


Figure 16. Using WGM to extract azimuthal anisotropy at each station. Original phase velocities varying with azimuth are plotted as colored dots to the left. The median velocity of each 10° azimuth window is a black dot. The median velocities of the 18 azimuth windows were modeled (red curve) to obtain anisotropy parameters for each station. a and b are the coefficients of the anisotropic model of Rayleigh wave (Figure 4 in Cao FH et al., 2020).

In addition to the velocity structure, the WGM has advantages for working on the surface wave with longer periods ($T > 40$ s) and can extract the wave propagation direction, amplitude variations with distance, and azimuth. Based on these parameters, attenuation can also be obtained (Equations 3-8 and 3-9).

5.2. WGM vs. Eikonal and Helmholtz tomographies

Lin FC et al. (2009, 2011) proposed Eikonal and Helmholtz tomographic methods to obtain local phase velocities and anisotropy from a dense array. These two methods are based on the Eikonal and Helmholtz equations, respectively, and yield phase velocity estimates. Eikonal and Helmholtz tomographies use travel time spatial gradients of certain phases extracted from cross-correlating waveforms, while the WGM uses the spatial wavefield gradients directly. Eikonal and Helmholtz tomographies do not analyze the radiation patterns with depth, as in the WGM. Liu YY and Holt (2015) summarized the relationship between the WGM and Eikonal and Helmholtz tomographies.

Eikonal tomography (Lin FC et al., 2009) is based on the 2D Eikonal equation:

$$\frac{1}{c'(x,y)^2} = |\nabla \tau(x,y)|^2 \quad (5-1)$$

where $c'(x,y)$ is the dynamic phase velocity (or apparent velocity) as a function of location (x,y) , $\tau(x,y)$ is the phase travel time that can be extracted by tracing the isochronous surface of the surface waves, and $\nabla \tau(x,y)$ is the spatial gradient of the phase time.

Helmholtz tomography (Lin FC and Ritzwoller, 2011) is based on the Helmholtz equation:

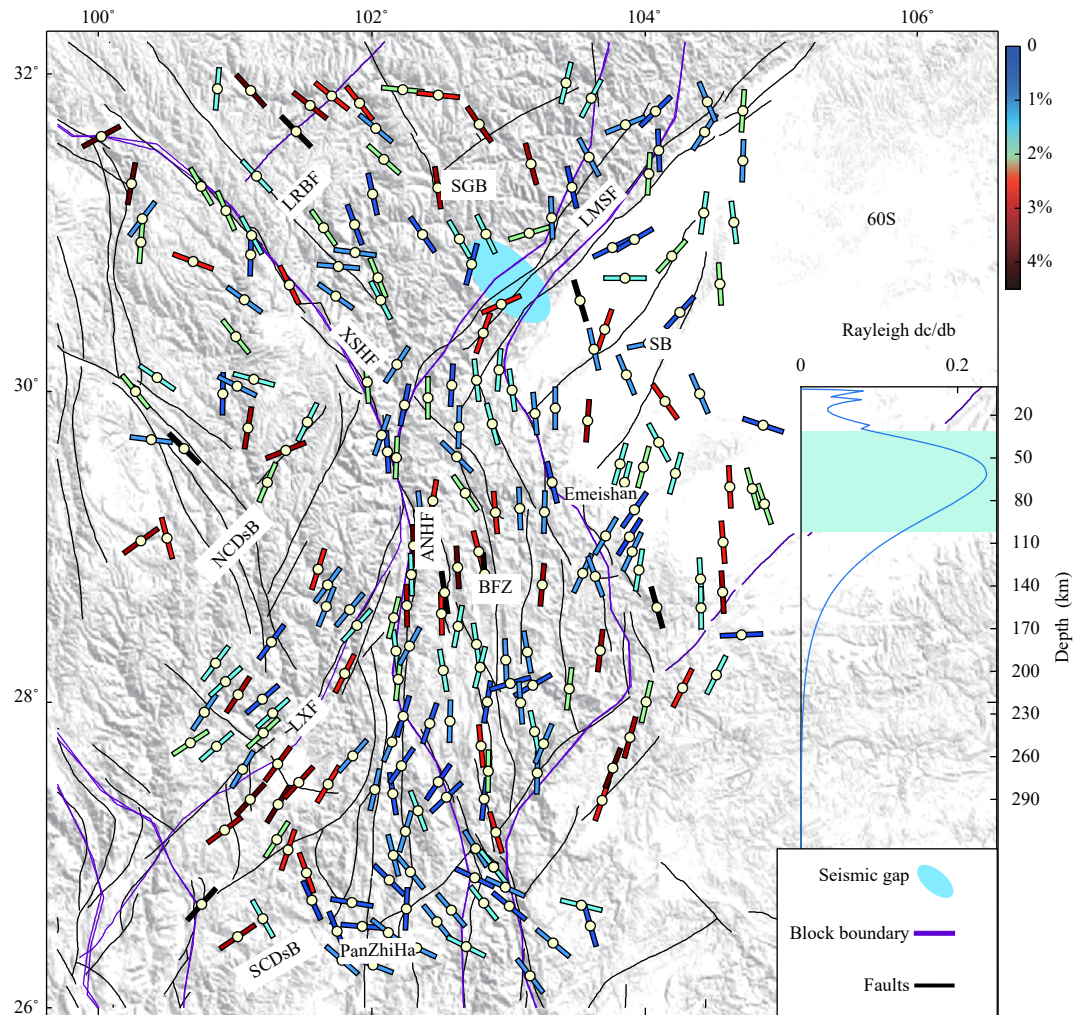
$$\frac{1}{c(x,y)^2} = |\nabla \tau(x,y)|^2 - \frac{\nabla^2 G(x,y)}{G(x,y) \omega^2} \quad (5-2)$$

where $G(x,y)$ is the wave amplitude (as in Equation 3-10) and $c(x,y)$ is the structural phase velocity (or corrected velocity as named by Lin FC and Ritzwoller (2011)). The main difference between Eikonal and Helmholtz tomography is that amplitude correction (second term in Equation 5.2) is considered in Helmholtz tomography to obtain the phase velocity.

The wave amplitude term $A = (A_x, A_y)$ determined by the WGM has an intrinsic relationship with the Helmholtz equation (Liu YY and Holt, 2015):

Table 2. Different array imaging methods currently in use.

Imaging Method	Data	Major Outputs	Network	Imaging Depth	Period (USArray)	Resolution
WGM	Noise (De Ridder and Curtis, 2017) and full waveform (Liang CT and Langston, 2009)	Velocity, anisotropy, attenuation, and radiation pattern	Linear (dense), 2D (dense), 3D, and vertical (dense)	Lithosphere	20–150 s (Porter et al., 2016)	Based on station density ($1.5 \times$ station spacing)
Ambient Noise Tomography (ANT)	Noise	Velocity Anisotropy	Linear and 2D	Crust	5–40 s	Based on ray path density (N/A)
Eikonal Tomography	Noise (Lin FC et al., 2009) and full waveform	Velocity and anisotropy	2D (dense)	Lithosphere	N/A	Based on station density (N/A)
Helmholtz Tomography	Noise and full waveform (Lin FC et al., 2011)	Velocity, anisotropy, and attenuation	2D (dense)	Lithosphere	20–100 s (Jin G and Gaherty, 2015)	Based on station density (N/A)

**Figure 17.** Azimuthal anisotropy at all stations for $T=60$ s. Color bar on the upper right is present amplitude of anisotropy. (Figure 8 in Cao FH et al., 2020).

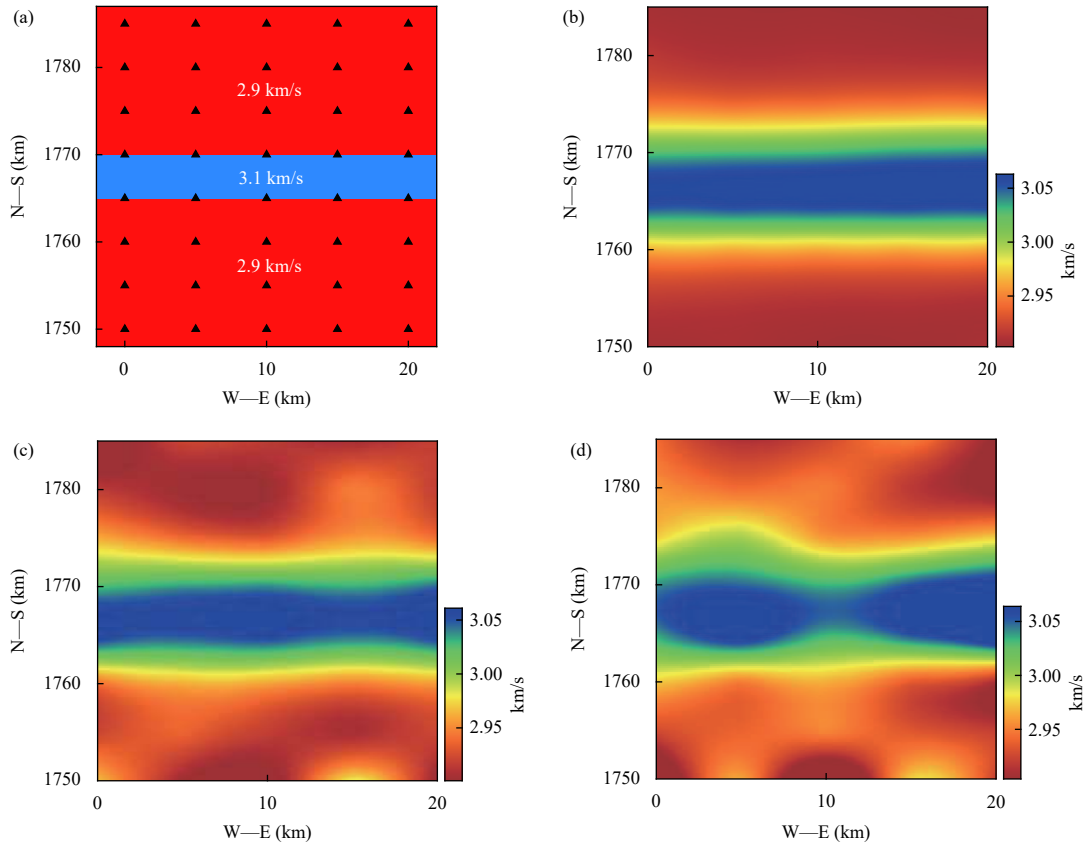


Figure 18. Resolution test, in which the real velocity model and velocity structure were computed using synthetic waveforms with different noise levels and a central period of 10 s (source location is (0, 0, 0)). (a) Real velocity model (different colors are different speed regions, triangles are array locations) with (b) no random noise added, (c) 4% random noise added, and (d) 8% random noise added (Figure 4 in Chang YN et al., 2022).

$$\mathbf{A} = \nabla \ln G = \frac{\nabla G}{G} \quad (5-3)$$

$$\mathbf{A}^2 + \nabla \cdot \mathbf{A} = \left(\frac{\nabla G}{G} \right)^2 + \frac{\nabla^2 G}{G} - \frac{(\nabla G)^2}{G^2} = \frac{\nabla^2 G}{G} \quad (5-4)$$

Based on Equations 3-15 and 3-16, $\mathbf{B} = -(p_x, p_y)$, which yields:

$$|\mathbf{B}| = |\mathbf{p}| = |\nabla \tau| \quad (5-5)$$

The corrected structural velocity is given as follows:

$$\frac{1}{c(x, y)^2} \approx |\mathbf{B}|^2 - \frac{\mathbf{A}^2 + \nabla \cdot \mathbf{A}}{\omega^2} \quad (5-6)$$

Equation (5-6) indicates that the phase velocity obtained by the WGM (Equation 3-18) may be contaminated by backscattering effects. By adding a correction term (second term in Equation 5-6), a structural phase velocity that is more indicative of the actual structure can be obtained. The phase velocity term is a combination of the \mathbf{A} and \mathbf{B} vectors. Lin FC and Ritzwoller (2011), Jin G and Gaherty (2015), and Liu YY and Holt (2015) all determined that the corrected phase velocity represents the structural velocity, which has better

constraints on the structure of the medium.

Similarly, Eikonal and Helmholtz tomographies are all essentially built upon dispersion curve inversion. Similar to the WGM, both Eikonal and Helmholtz tomographies can be used for long periods. As shown in Figure 22, although, the WGM treats the phase as a constant (first-order approximation of the spatial wavefield gradient) over a small range, the phase velocity and anisotropy estimated using the WGM are remarkably consistent with those estimated using Eikonal tomography (second order spatial gradient of the phase travel time). The major advantage of the WGM is its ability to extract geometrical spreading and radiation patterns. In addition, the WGM has more flexible applications than Eikonal or Helmholtz tomographies; thus, the WGM can be applied to more network types (Table 1), seismic phases (Table 1), and can be used to identify body wave arrival times (Sollberger et al., 2016).

6. Conclusions

In this review, we have outlined the theoretical foundations, technical development, and major

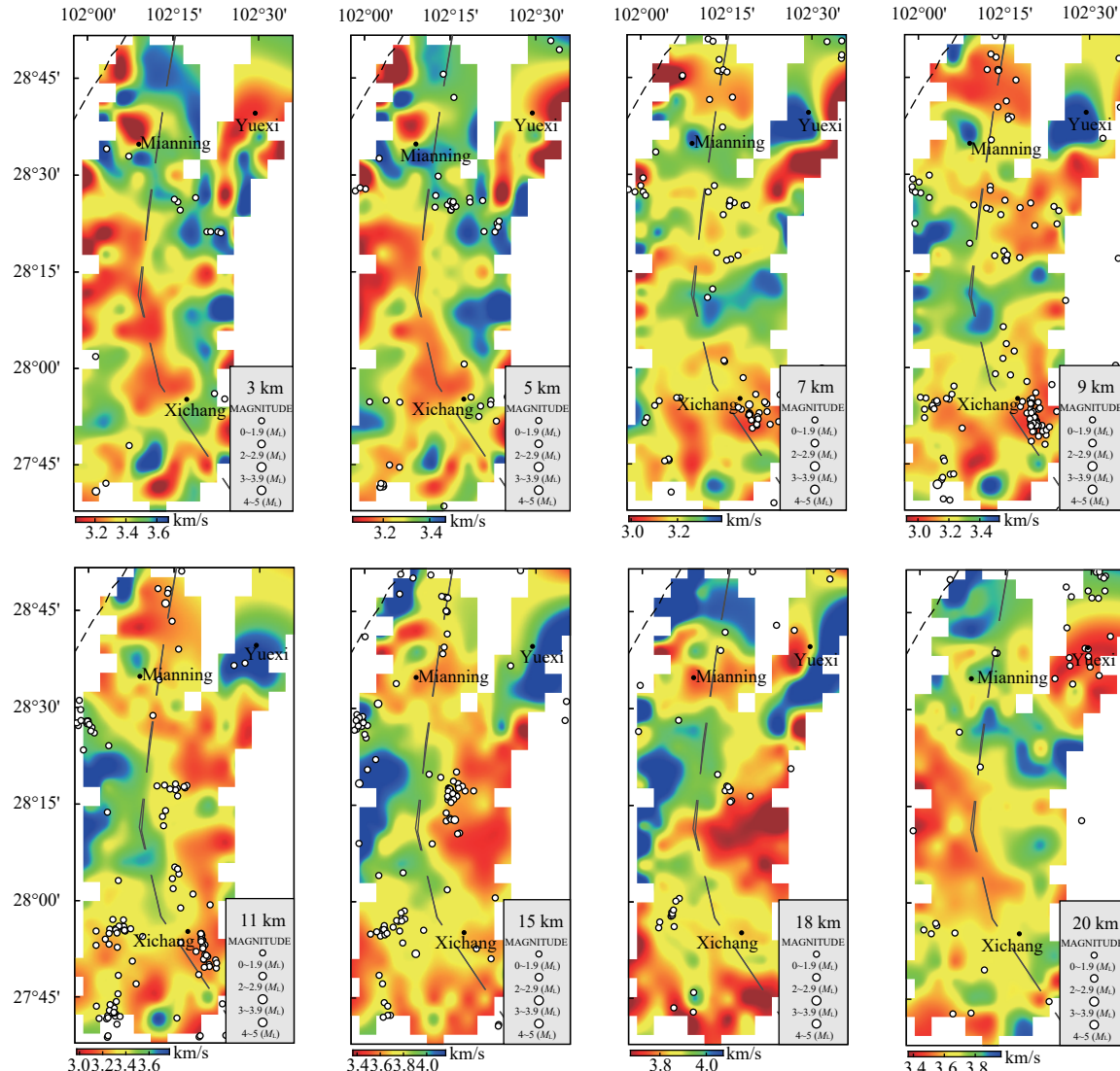


Figure 19. S wave velocity maps at depths of 3, 5, 7, 9, 11, 15, 18, and 20 km. Black dashed lines are block boundaries and circles are earthquakes that occurred at each depth. The earthquakes on each map are those with depths 1 km above and below the depth threshold. For example, the seismic source depths in the 3 km depth map are located at 2–4 km (Figure 7 in Chang YN et al., 2022).

applications of the WGM and compared it with other major array imaging methods. The WGM uses the spatial wavefield gradients to obtain 4 major attributes: phase velocity, wave directionality, geometrical spreading, and radiation pattern. These attributes can be used to further extract the strain and rotation tensors (Langston and Liang CT, 2008; Sollberger et al., 2016), and can also be used to extract structural information such as velocity, anisotropy, attenuation, and impedance, among others.

The WGM can be applied to the full waveform (Langston, 2007a, b, c), body waves (Langston and Ayele, 2016; Sollberger et al., 2016), or surface waves (Liang CT and Langston, 2009; Porter et al., 2016; Cao FH et al., 2020). It can also be applied to ambient noise data (De

Ridder and Curtis, 2017).

Spatial gradients can be computed in various ways, including the weighted inversion (Liang CT and Langston, 2009), wavefield bi-cubic spline interpolation (Liu YY and Holt, 2015), and Taylor expansion-based wavefield gridding (Maeda et al., 2016) methods. The advantages and disadvantages of these three methods may require further analysis.

The WGM attributes based on spatial gradients can also be computed in several ways, including the frequency domain (Langston, 2007a), Hilbert transform (Langston, 2007c), and linear inversion (Liu YY and Holt, 2015) methods. The Hilbert transform method may have the highest temporal resolution among these methods.

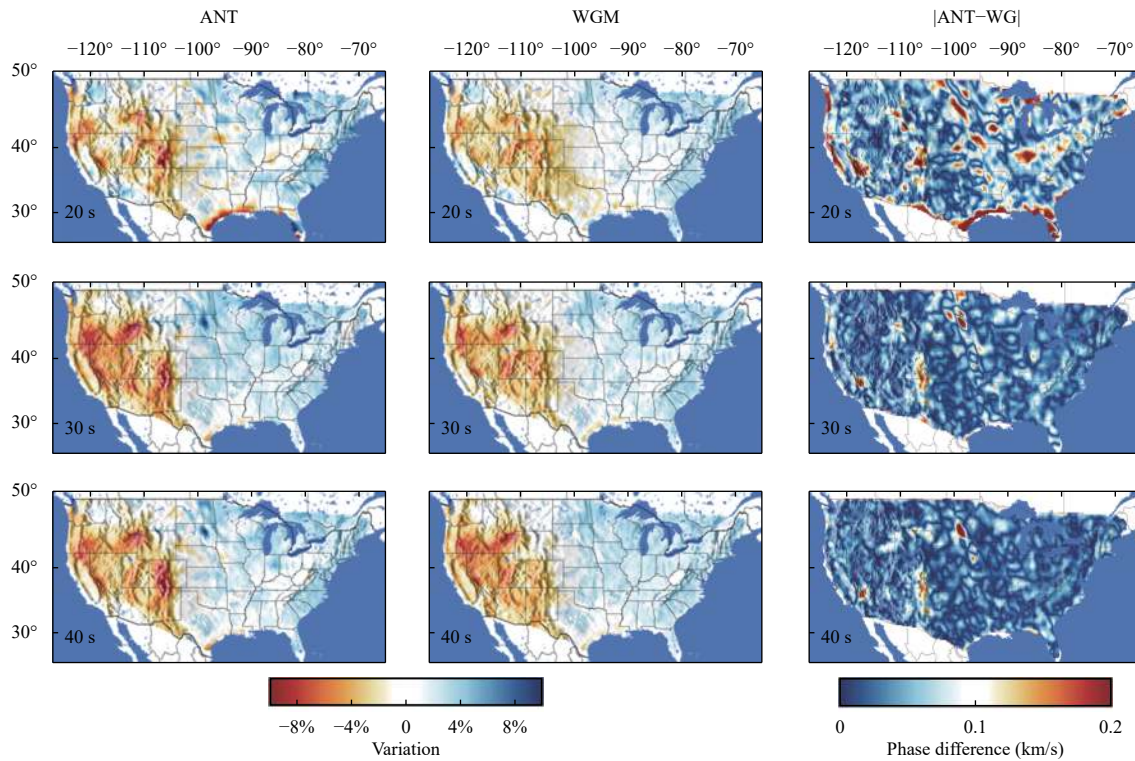


Figure 20. Absolute values of the differences between phase velocities calculated using ANT and the WGM. Maps in the left column the middle column are the phase velocity of different periods inverted by the ANT the WGM, respectively. Maps in the right column showing absolute value of the difference between phase velocity calculated by ANT and WGM (Figures S1 and S2 in [Porter et al., 2016](#)).

The WGM has been applied to arrays with a large range of scales. The USArray (average spacing of 70 km) may be the largest array to which the WGM has been applied, while the mini gradiometer (station spacing of less than 1 m) designed by Barker and Langston (2016) could be the smallest array to which the WGM has been applied. The frequency band ranges from tens of Hz to 150 s.

The horizontal resolution of the WGM is $\sim 1\text{--}1.5$ times the station spacing. Although the properties are calculated for grids that can be denser than the array, the resolution of the WGM may also be affected by the smoothing factor and sub-array radius. ,

Similar to ANT, and Eikonal and Helmholtz tomographies, the WGM can also be reduced to the inversion of dispersion curves. However, the WGM has a few advantages for imaging deep Earth structures:

(1) For regional arrays (e.g., USArray and ChinArray), the imaging depth of the WGM can be as deep as the entire lithosphere or deeper. As shown by Porter et al. (2016), the WGM can image to a depth of 150 km. This is because the WGM works for the longest periods that an instrument can record. However, the period band for ANT is usually less than 40 s owing to the limited frequency band of the noise source; therefore, its imaging depth is limited to the crust.

(2) The WGM has the potential to resolve 3D attenuation structures, as it can extract geometrical spreading attributes. Langston and Ayele. (2016) determined the attenuation for the SAFOD profile using the WGM. The attenuation is theoretically included in the geometrical spreading term (Equation 3-9).

(3) The WGM has the potential to be used as a tool for measuring strain and rotation tensors ([Langston and Liang CT, 2008](#); [Sollberger et al., 2016](#); Equations 4-6 and 4-7). This would expand the usability of general seismographs.

(4) The WGM can be used as a tool to identify major phases. The WGM attributes fluctuate substantial at the phase arrival times. Langston (2007c) used this property to identify the sedimentary phase, whereas Sollberger et al. (2016) applied the WGM to identify shear waves by their rotation energy variations.

Although dramatic achievements have been made, improvements are still required:

(1) Applying the WGM to all possible phases. The applications of the WGM are still largely concentrated on surface waves. Applications to other phases, including abundant reflected and refracted phases from deep interfaces (e.g., tPcP, PKP, and Sdiff) could be used to study the deep structure of the Earth and wave propagation

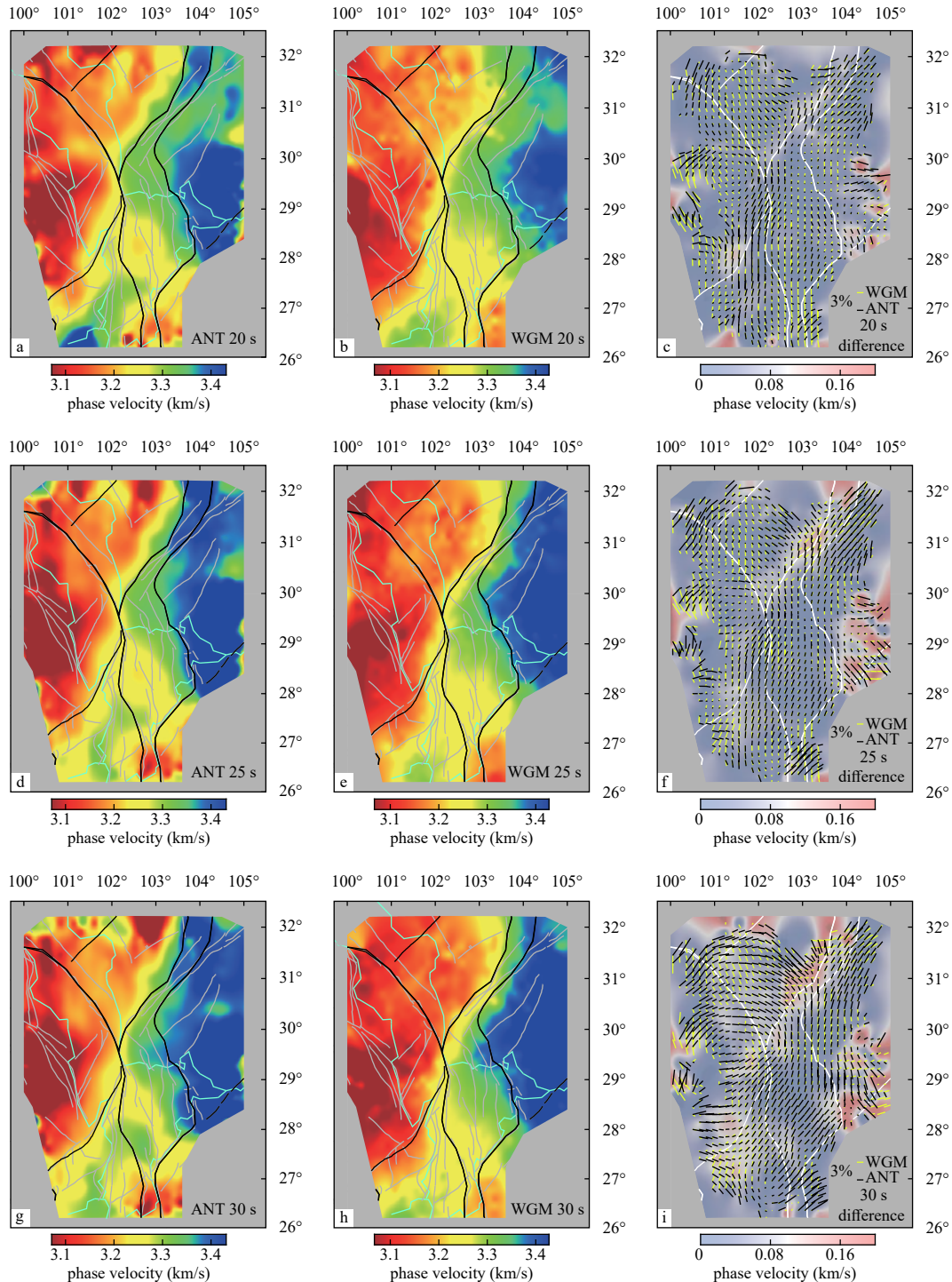


Figure 21. Comparison of the results calculated using ANT and the WGM. (a), (d), and (g) are phase velocity maps calculated using ANT. (b), (e), and (h) are phase velocity maps calculated using the WGM. The base maps in (c), (f), and (i) show the absolute values of the differences between the two methods. Black and yellow bars represent the Rayleigh wave azimuthal anisotropy calculated using ANT and the WGM (Figure S7 in Cao FH et al., 2023).

properties. The application of the WGM to Moonquake data is a good example of this.

(2) Inverting for 3D attenuation. Langston and Ayele (2016) extracted the attenuation using the SAFOD seismic

array. However, separating intrinsic attenuation from the focusing and de-focusing effect remains challenging. Inverting for 3D attenuation would be a major development for the WGM.

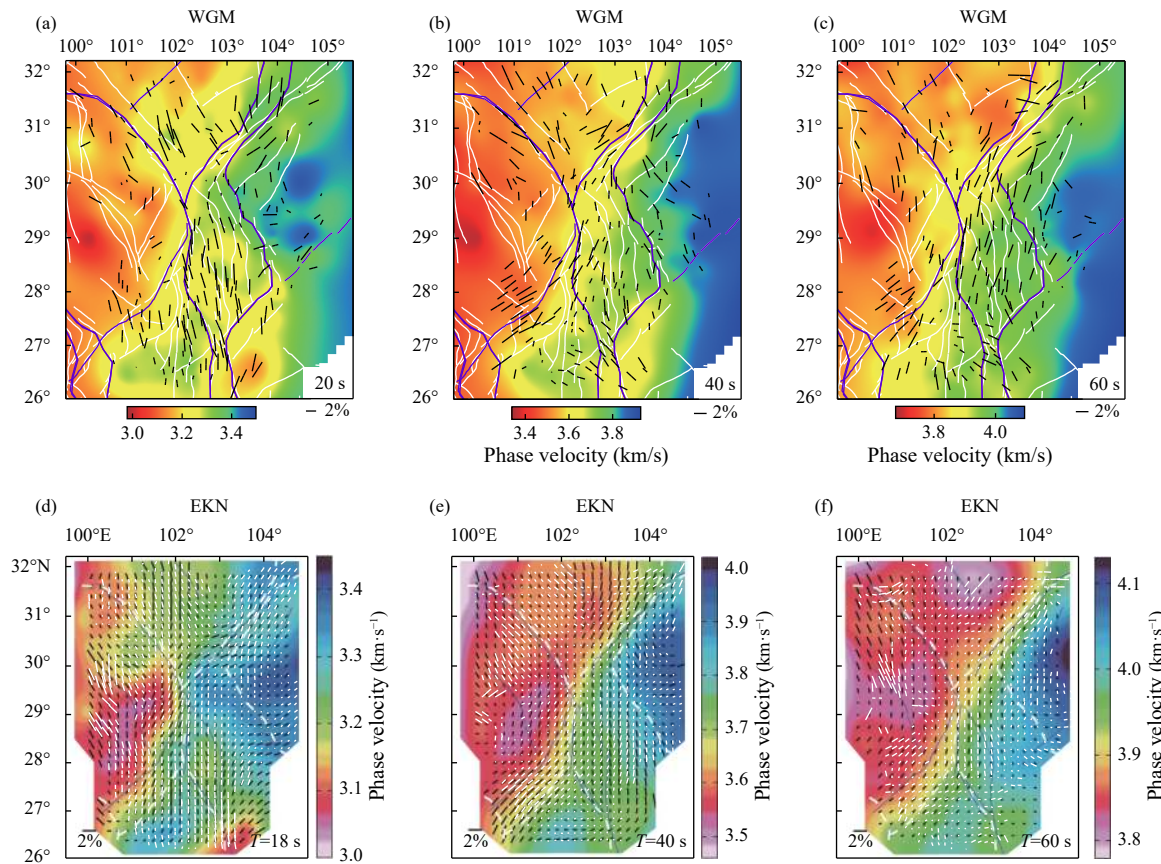


Figure 22. Comparisons of Rayleigh wave phase velocities and azimuthal anisotropy calculated using the WGM and Eikonal tomography in the southeastern margin of the Tibetan plateau. (a)–(c) Results for periods of 20, 40, and 60 s calculated using the WGM based on the weight inversion method (modified from Figures 5–8 in Cao FH et al., 2020). (d)–(f) Results for periods of 20, 40, and 60 s calculated using Eikonal tomography (velocity shown on base maps and anisotropy shown as black bars, modified from Figure 7 in Wang HF et al., 2020). White bars are the azimuthal anisotropy calculated using the WGM based on the gridding method (modified from Figure 10 in Cao FH et al., 2023).

(3) Inverting for radial anisotropy. Inverting for 3D azimuthal anisotropy based on the WGM has been successful (Cao FH et al., 2022); however, its potential to extract 3D radial anisotropy has not been tested. Zhou L et al. (2017) applied the WGM to the vertical, radial, and transverse components of the USArray and found that the phase velocities for SH and SV waves were generally consistent, but the subtle differences may reveal the radial anisotropy. Inverting for 3D radial anisotropy is a new research direction that should be addressed in the future.

(4) Joint analysis with other techniques. Porter et al. (2016) jointly inverted ANT and the WGM. Cao FH et al. (2023) jointly inverted dispersion curves obtained using the WGM and ANT, and receiver functions. Because the different methods may have different sensitivities, combining these techniques may provide more constraints to address tectonic problems.

(5) Application to datasets in the oil and gas industry. The oil and gas industry has massive datasets with dense

2D arrays. Applying the WGM to these datasets may not only add new value to existing data but may also create new opportunities for the WGM.

(6) Application to data collected by optical fibers. Distributed acoustic sensing (DAS) is becoming more commonly used in the energy industry and earthquake research. Because DAS sampling can be extremely dense according to the purpose of the study, these datasets are ideal for applying the WGM.

References

- Aki K and Lee WHK (1976). Determination of three-dimensional velocity anomalies under a seismic array using first P arrival times from local earthquakes: 1. A homogeneous initial model. *J Geophys Res* **81**(23): 4381–4399 <https://doi.org/10.1029/JB081i023p04381>.
- Aki K, Christoffersson A and Husebye ES (1977). Determination of the three-dimensional seismic structure of the lithosphere. *J Geophys Res* **82**(2): 277–296 <https://doi.org/10.1029/JB082i002p0277>

- [JB082i002p00277](#).
- Ammon CJ, Zucca J and Kasameyer P (1989). An *S*-to-*P* converted phase recorded near Long Valley/Mono Craters Region, California. *J Geophys Res* **94**(B12): 17721–17727 <https://doi.org/10.1029/jb094b12p17721>.
- Barker LM and Langston CA (2016). Small-scale array experiments in seismic-wave gradiometry. *Seismol Res Lett* **87**(5): 1091–1103 <https://doi.org/10.1785/0220160040>.
- Barmin MP, Ritzwoller MH and Levshin AL (2001). A fast and reliable method for surface wave tomography. *Pure Appl Geophys* **158**(8): 1351–1375 <https://doi.org/10.1007/PL00001225>.
- Bensen GD, Ritzwoller MH and Shapiro NM (2008). Broadband ambient noise surface wave tomography across the United States. *J Geophys Res* **113**(B5): B05306 <https://doi.org/10.1029/2007JB005248>.
- Bissig F, Khan A, Tauzin B, Sossi PA, Munch FD and Giardini D (2021). Multifrequency inversion of Ps and Sp receiver functions: Methodology and application to USArray data. *J Geophys Res: Solid Earth* **126**(2): e2020JB020350 <https://doi.org/10.1029/2020JB020350>.
- Burdick S, Li C, Martynov V, Cox T, Eakins J, Mulder T, Astiz L, Vernon FL, Pavlis GL and Van Der Hilst RD (2008). Upper mantle heterogeneity beneath North America from travel time tomography with global and USArray transportable array data. *Seismol Res Lett* **79**(3): 384–392 <https://doi.org/10.1785/gssrl.79.3.384>.
- Campillo M and Paul A (2003). Long-range correlations in the diffuse seismic coda. *Science* **299**(5606): 547–549 <https://doi.org/10.1126/science.1078551>.
- Cao FH, Liang CT, Zhou L and Zhu JS (2020). Seismic azimuthal anisotropy for the southeastern Tibetan Plateau extracted by wave gradiometry analysis. *J Geophys Res: Solid Earth* **125**(5): e2019JB018395 <https://doi.org/10.1029/2019JB018395>.
- Cao FH, Liang CT, Yang YH, Zhou L, Liu ZQ and Liu Z (2023). 3D velocity and anisotropy of the southeastern Tibetan plateau extracted by joint inversion of wave gradiometry, ambient noise, and receiver function. *Tectonophysics* **848**: 229690 <https://doi.org/10.1016/j.tecto.2022.229690>.
- Cao RK, Earp S, De Ridder SAL, Curtis A and Galetti E (2020). Near-real-time near-surface 3D seismic velocity and uncertainty models by wavefield gradiometry and neural network inversion of ambient seismic noise. *Geophysics* **85**(1): KS13–KS27 <https://doi.org/10.1190/geo2018-0562.1>.
- Challu C, Poppeliers C, Punoševac P and Dubrawski A (2021). Explosion discrimination using seismic gradiometry and spectral filtering of data. *Bull Seismol Soc Am* **111**(3): 1365–1377 <https://doi.org/10.1785/0120200304>.
- Chang YN, Liang CT, Cao FH, Zhou L, Liao JT, Lu WF and Wang CL (2022). Seismic velocity structure for the Anninghe-Zemuhe fault zone by wave gradiometry analysis. *Chin J Geophys* **65**(8): 2886–2903 <https://doi.org/10.6038/cjg2022P0731> (in Chinese with English abstract).
- Chen CX, Zhao DP, Tian Y, Wu SG, Hasegawa A, Lei JS, Park JH and Kang IB (2017). Mantle transition zone, stagnant slab and intraplate volcanism in northeast Asia. *Geophys J Int* **209**(1): 68–85 <https://doi.org/10.1093/gji/ggw491>.
- Chavarria JA, Goertz A, Karrenbach M, Paulsson B, Milligan P, Soutyrine, Hardin V, Dushman D and LaFlame L (26). The use of VSP techniques for fault zone characterization: An example from the San Andreas Fault. *The Leading Edge* **6**: 770–776 <https://doi.org/10.1190/1.2748495>.
- De Ridder SAL and Biondi BL (2015). Near-surface Scholte wave velocities at Ekofisk from short noise recordings by seismic noise gradiometry. *Geophys Res Lett* **42**(17): 7031–7038 <https://doi.org/10.1002/2015GL065027>.
- De Ridder SAL and Curtis A (2017). Seismic gradiometry using ambient seismic noise in an anisotropic Earth. *Geophys J Int* **209**(2): 1168–1179 <https://doi.org/10.1093/gji/ggx073>.
- Edme P and Yuan SH (2016). Local dispersion curve estimation from seismic ambient noise using spatial gradients. *Interpretation* **4**(3): SJ17–SJ27 <https://doi.org/10.1190/INT-2016-0003.1>.
- Fang HJ, Yao HJ, Zhang HJ, Huang YC and Van Der Hilst RD (2015). Direct inversion of surface wave dispersion for three-dimensional shallow crustal structure based on ray tracing: methodology and application. *Geophys J Int* **201**(3): 1251–1263 <https://doi.org/10.1093/gji/ggv080>.
- Fischer KM, Li AB, Forsyth DW, and Hung SH (2005). Imaging three-dimensional anisotropy with broadband seismometer arrays. In: Levander A, and Nolet G eds. *Seismic Earth: Array Analysis of Broadband Seismograms*. AGU, Washington. <https://doi.org/10.1029/157GM07>.
- Gao SS and Liu KH (2009). Significant seismic anisotropy beneath the southern Lhasa Terrane, Tibetan Plateau. *Geochem Geophys Geosyst* **10**(2): Q02008 <https://doi.org/10.1029/2008GC002227>.
- Herrmann RB, and Ammon CJ (2004). *Surface Waves, Receiver Functions and Crustal Structure, Computer Programs in Seismology*. Saint Louis University, Saint Louis, pp. 133, 135.
- Hetényi G, Molinari I, Clinton J, Bokelmann G, Bondár I, Crawford WC, Dessa JX, Doubre C, Friederich W, Fuchs F, Giardini D, Grácer Z, Handy MR, Herak M, Jia Y, Kissling E, Kopp H, Korn M, Margheriti L, Meier T, Mucciarelli M, Paul A, Pesaresi D, Piromallo C, AlpArray Seismic Network Team, AlpArray OBS Cruise Crew, AlpArray Working Group (2018). The AlpArray seismic network: a large-scale European experiment to image the Alpine Orogen. *Surv Geophys* **39**(5): 1009–1033 <https://doi.org/10.1007/s10712-018-9472-4>.
- Hickman S and Zoback M (2004). Stress orientations and magnitudes in the SAFOD pilot hole. *Geophys Res Lett* **31**(5): L15S12 <https://doi.org/10.1029/2004GL020043>.
- Jin G and Gaherty JB (2015). Surface wave phase-velocity tomography based on multichannel cross-correlation. *Geophys J Int* **201**(3): 1383–1398 <https://doi.org/10.1093/gji/ggv079>.
- Kästle ED, Molinari I, Boschi L, Kissling E and the AlpArray

- Working Group (2022). Azimuthal anisotropy from eikonal tomography: example from ambient-noise measurements in the AlpArray network. *Geophys J Int* **229**(1): 151–170 <https://doi.org/10.1093/gji/ggab453>.
- Keranen KM, Weingarten M, Abers GA, Bekins BA and Ge S (2014). Sharp increase in central Oklahoma seismicity since 2008 induced by massive wastewater injection. *Science* **345**(6195): 448–451 <https://doi.org/10.1126/science.1255802>.
- Kim YC, Hurt Jr WB, Maher LJ and Stanch PJ (1997). Hybrid migration: a cost-effective 3-D depth-imaging technique. *Geophysics* **62**(2): 568–576 <https://doi.org/10.1190/1.1444166>.
- Knopoff L, Mueller S and Pilant WL (1966). Structure of the crust and upper mantle in the ALPS from the phase velocity of Rayleigh waves. *Bull Seismol Soc Am* **56**(5): 1009–1044 <https://doi.org/10.1785/BSSA0560051009>.
- Krischer L, Fichtner A, Boehm C and Igel H (2018). Automated large-scale full seismic waveform inversion for North America and the North Atlantic. *J Geophys Res: Solid Earth* **123**(7): 5902–5928 <https://doi.org/10.1029/2017JB015289>.
- Langston CA (1979). Structure under Mount Rainier, Washington, inferred from teleseismic body waves. *J Geophys Res* **84**(B9): 4749–4762 <https://doi.org/10.1029/jb084ib09p04749>.
- Langston CA (2007a). Spatial gradient analysis for linear seismic arrays. *Bull Seismol Soc Am* **97**(1B): 265–280 <https://doi.org/10.1785/0120060100>.
- Langston CA (2007b). Wave gradiometry in two dimensions. *Bull Seismol Soc Am* **97**(2): 401–416 <https://doi.org/10.1785/0120060138>.
- Langston CA (2007c). Wave gradiometry in the time domain. *Bull Seismol Soc Am* **97**(3): 926–933 <https://doi.org/10.1785/0120060152>.
- Langston CA and Liang CT (2008). Gradiometry for polarized seismic waves. *J Geophys Res: Solid Earth* **113**(B8): B08305 <https://doi.org/10.1029/2007JB005486>.
- Langston CA and Ayele MM (2016). Vertical seismic wave gradiometry: application at the San Andreas fault observatory at depth. *Geophysics* **81**(3): D233–D243 <https://doi.org/10.1190/GEO2015-0404.1>.
- Liang CT and Langston CA (2009). Wave gradiometry for USArray: Rayleigh waves. *J Geophys Res: Solid Earth* **114**(B2): B02308 <https://doi.org/10.1029/2008JB005918>.
- Liang CT, Liu ZQ, Hua Q, Wang L, Jiang NB and Wu J (2020). The 3D seismic azimuthal anisotropies and velocities in the eastern Tibetan plateau extracted by an azimuth-dependent dispersion curve inversion method. *Tectonics* **39**(4): e2019T C005747 <https://doi.org/10.1029/2019TC005747>.
- Lin FC, Ritzwoller MH and Snieder R (2009). Eikonal tomography: surface wave tomography by phase front tracking across a regional broad-band seismic array. *Geophys J Int* **177**(3): 1091–1110 <https://doi.org/10.1111/j.1365-246X.2009.04105.x>.
- Lin FC and Ritzwoller MH (2011). Helmholtz surface wave tomography for isotropic and azimuthally anisotropic structure. *Geophys J Int* **186**(3): 1104–1120 <https://doi.org/10.1111/j.1365-246X.2011.05070.x>.
- Lippitsch R, Kissling E and Ansorge J (2003). Upper mantle structure beneath the Alpine orogen from high-resolution teleseismic tomography. *J Geophys Res* **108**(B8): 2376 <https://doi.org/10.1029/2002JB002016>.
- Liu QY, Chen JH, Li SC, Li Y, Guo B, Wang J and Qi SH (2008). The M_S 8.0 Wenchuan earthquake: Preliminary results from the western Sichuan mobile seismic array observations. *Seismol Geol* **30**(3): 584–596 <https://doi.org/10.3969/j.issn.0253-4967.2008.03.002> (in Chinese with English abstract).
- Liu QY, Van Der Hilst RD, Li Y, Yao HJ, Chen JH, Guo B, Qi SH, Wang J, Huang H and Li SC (2014). Eastward expansion of the Tibetan plateau by crustal flow and strain partitioning across faults. *Nat Geosci* **7**(5): 361–365 <https://doi.org/10.1038/ngeo2130>.
- Liu YY and Holt WE (2015). Wave gradiometry and its link with helmholtz equation solutions applied to USArray in the eastern U. S. *J Geophys Res: Solid Earth* **120**(8): 5717–5746 <https://doi.org/10.1002/2015JB011982>.
- Maeda T, Nishida K, Takagi R and Obara K (2016). Reconstruction of a 2D seismic wavefield by seismic gradiometry. *Prog Earth Planet Sci* **3**(1): 31 <https://doi.org/10.1186/s40645-016-0107-4>.
- Molinari I, Clinton J, Kissling E, Hetényi G, Giardini D, Stipčević J, Dasović I, Herak M, Šipka V, Wéber Z, Grácer Z, Solarino S, the Swiss-AlpArray Field Team and the AlpArray Working Group (2016). Swiss-AlpArray temporary broadband seismic stations deployment and noise characterization. *Adv Geosci* **43**: 15–29 <https://doi.org/10.5194/adgeo-43-15-2016>.
- Park CB, Miller RD and Xia JH (1999). Multichannel analysis of surface waves. *Geophysics* **64**(3): 800–808 <https://doi.org/10.1190/1.1444590>.
- Poppeliers C (2010). Seismic wave gradiometry using the wavelet transform: application to the analysis of complex surface waves recorded at the Glendora array, Sullivan, Indiana, USA. *Bull Seismol Soc Am* **100**(3): 1211–1224 <https://doi.org/10.1785/0120090304>.
- Poppeliers C (2011). Multiwavelet seismic-wave gradiometry. *Bull Seismol Soc Am* **101**(5): 2108–2121 <https://doi.org/10.1785/0120100226>.
- Poppeliers C, Punoševac P and Bell T (2013). Three-dimensional seismic-wave gradiometry for scalar waves. *Bull Seismol Soc Am* **103**(4): 2151–2160 <https://doi.org/10.1785/0120120224>.
- Porter R, Liu YY and Holt WE (2016). Lithospheric records of Orogeny within the continental U. S. *Geophys Res Lett* **43**(1): 144–153 <https://doi.org/10.1002/2015GL066950>.
- Qiu HR, Lin FC and Ben-Zion Y (2019). Eikonal tomography of the Southern California plate boundary region. *J Geophys Res: Solid Earth* **124**(9): 9755–9779 <https://doi.org/10.1029/2019JB017806>.
- Robertsson JOA and Curtis A (2002). Wavefield separation using densely deployed three-component single-sensor groups in

- landsurface-seismic recordings. *Geophysics* **67**(5): 1624–1633 <https://doi.org/10.1190/1.1512809>.
- Savazzi S, and Spagnolin U (2009). Synchronous ultra-wide band wireless sensors networks for oil and gas exploration. In: 2009 IEEE Symposium on Computers and Communications. IEEE, Sousse, pp. 907–912. <https://doi.org/10.1109/ISCC.2009.5202244>.
- Shapiro NM, Campillo M, Stehly L and Ritzwoller MH (2005). High-resolution surface-wave tomography from ambient seismic noise. *Science* **307**(5715): 1615–1618 <https://doi.org/10.1126/science.1108339>.
- Sollberger D, Schmelzbach C, Robertsson JOA, Greenhalgh SA, Nakamura Y and Khan A (2016). The shallow elastic structure of the lunar crust: new insights from seismic wavefield gradient analysis. *Geophys Res Lett* **43**(19): 10078–10087 <https://doi.org/10.1002/2016GL070883>.
- Sollberger D, Schmelzbach C, Manukyan E, Greenhalgh SA, Van Renterghem C and Robertsson JOA (2019). Accounting for receiver perturbations in seismic wavefield gradiometry. *Geophys J Int* **218**(3): 1748–1760 <https://doi.org/10.1093/gji/ggz258>.
- Spudich P, Steck LK, Hellweg M, Fletcher JB and Baker LM (1995). Transient stresses at Parkfield, California, produced by the $M7.4$ Landers earthquake of June 28, 1992: Observations from the UPSAR dense seismograph array. *J Geophys Res* **100**(B1): 675–690 <https://doi.org/10.1029/94JB02477>.
- Tromp J (2020). Seismic wavefield imaging of Earth's interior across scales. *Nat Rev Earth Environ* **1**(1): 40–53 <https://doi.org/10.1038/s43017-019-0003-8>.
- Van Der Lee S and Nolet G (1997). Upper mantle S velocity structure of North America. *J Geophys Res* **102**(B10): 22815–22838 <https://doi.org/10.1029/97JB01168>.
- Van Renterghem C, Schmelzbach C, Sollberger D and Robertsson JOA (2018). Spatial wavefield gradient-based seismic wavefield separation. *Geophys J Int* **212**(3): 1588–1599 <https://doi.org/10.1093/gji/ggx499>.
- Vinnik LP (1977). Detection of waves converted from P to SV in the mantle. *Phys Earth Planet Inter* **15**(1): 39–45 [https://doi.org/10.1016/0031-9201\(77\)90008-5](https://doi.org/10.1016/0031-9201(77)90008-5).
- Wang HF, Wu JP, Zhou SY and Feng T (2020). Rayleigh wave azimuthal anisotropy in western Sichuan region. *Acta Seismol Sin* **42**(3): 293–305 <https://doi.org/10.11939/jass.20190103> (in Chinese with English abstract).
- Wang Y, Liu JS, Shen CM, Deng B, Su WJL, Chen QF and Li JL (2022). Seismic ambient noise tomography with dense linear arrays and its application in the exploration of the Woxi Au-Sb-W deposit in Hunan. *Geol J China Univ* **28**(3): 402–413 <https://doi.org/10.16108/j.issn1006-7493.2021008> (in Chinese with English abstract).
- Whitham GB (1999). Linear and Nonlinear Waves: Whitham/Linear. John Wiley & Sons, Inc., New York, pp. 209–262. <https://doi.org/10.1002/9781118032954>.
- Xia JH, Miller RD and Park CB (1999). Estimation of near-surface shear-wave velocity by inversion of Rayleigh waves. *Geophysics* **64**(3): 691–700 <https://doi.org/10.1190/1.1444578>.
- Yang W, Chen GY, Meng LY, Zang Y, Zhang HJ and Li JL (2021). Determination of the local magnitudes of small earthquakes using a dense seismic array in the Changning–Zhaotong Shale Gas Field, Southern Sichuan Basin. *Earth Planet Phys* **5**(6): 532–546 <https://doi.org/10.26464/epp2021026>.
- Yang YJ, Ritzwoller MH, Levshin AL and Shapiro NM (2007). Ambient noise Rayleigh wave tomography across Europe. *Geophys J Int* **168**(1): 259–274 <https://doi.org/10.1111/j.1365-246X.2006.03203.x>.
- Yao HJ, Van Der Hilst RD and De Hoop MV (2006). Surface-wave array tomography in SE Tibet from ambient seismic noise and two-station analysis — I. Phase velocity maps. *Geophys J Int* **166**(2): 732–744 <https://doi.org/10.1111/j.1365-246X.2006.03028.x>.
- Zhang H, Mi BB, Xi CQ, Liu Y, Guan B and Ning L (2022). Extraction of surface-wave phase velocities from ambient noise in the presence of local noise sources based on matched-field processing. *J Appl Geophys* **204**: 104755 <https://doi.org/10.1016/j.jappgeo.2022.104755>.
- Zhang L, Fang LH, Wang WL and Lv ZY (2020). Seismic phase picking in China Seismic Array using a deep convolutional neuron network. *Earthq Sci* **33**(2): 72–81 <https://doi.org/10.2938/eqs-2020-0072-03>.
- Zhou L, Liang CT and Yang YH (2017). Application of three-component seismic-wave gradiometry for the Central and Eastern United States. *Chin J Geophys* **60**(9): 3352–3367 <https://doi.org/10.6038/cjg20170907> (in Chinese with English abstract).
- Zoback M, Hickman SH, Ellsworth E and the SAFOD Science Team (2011). Scientific drilling into the San Andreas fault zone – an overview of SAFOD's first five years. *Sci Drill* **11**: 14–28 <https://doi.org/10.2204/iodp.sd.11.02.2011>.